University of Lisbon

Faculty of Sciences
Department of Physics

Experimental advances on alpha nuclear potentials for the astrophysical p-process

---

Author:

André José Neves Marques de Ornelas

Master's Thesis Dissertation

Master in Physic's Engineering

2012

University of Lisbon

Faculty of Sciences
Department of Physics

Experimental advances on alpha nuclear potentials for the astrophysical p-process

---

Author:

André José Neves Marques de Ornelas

Master's Thesis Dissertation

Master in Physic's Engineering

Supervisors:

Dr. Daniel Galaviz

Dr. Gy. Gyürky

2012

To my parents Ana and Manuel, my family (my cousins, that helped me along the way to overcome many obstacles) , my friends, with special care to Andreia Cardoso, Ana Henriques, Catarina Duarte, Alexandre Lopes, Vanessa Gil, João José and many others... , my many teachers that inspired me and for all the people that have supported me. Without you I couldn't have accomplished my goal.
To all, my deepest thanks.

It should be possible to explain the laws of physics to a barmaid.
Albert Einstein

"It is wrong to think that the task of physics is to find out how Nature is. Physics concerns what we say about Nature."
Niels Bohr

Abstract

The subject of the present Master Thesis "Experimental advances on alpha nuclear potentials for the astrophysical p-process" is the experimental activity performed during my training period at ATOMKI in Debrecen, Hungary, under the ERASMUS program tutelage.

In this dissertation the process will be described for preparation of the experiment of elastic α scattering from ^{64}Zn, ^{113}In and ^{115}In targets. The electric connections, detectors and their calibration, pre-amplifiers, amplifiers, and the overall experimental setup is described in detail.

The results of this experiment will allow the calculation of the cross section of the studied elements, perform the comparison of the experimental data with theoretical predictions of the most accepted models for global α–nucleus potentials . The results will also allow for a detailed study about the "families" of local α–nucleus potentials in order to improve the predictive power of the existent theoretical models and the overall knowledge in the area of astrophysics.

Keywords: p-process, supernova type II, elastic α scattering, cross-section, α–nucleus potential.

Resumo

A dissertação "Experimental advances on alpha nuclear potentials for the astrophysical p-process" reflecte a actividade experimental realizada durante o período de estágio no ATOMKI, em Debrecen na Hungria, realizado sobre alçada do programa ERASMUS.

Nesta dissertação será descrito o processo de preparação para a experiência de dispersão de partículas α em alvos de ^{64}Zn, ^{113}In e ^{115}In. As ligações eléctricas, detectores e respectiva calibração, pré-amplificadores, amplificadores, assim como a resultante montagem experimental serão descritas em detalhe.

Os resultados da experiência de dispersão de partículas α irão permitir calcular a secção eficaz dos elementos estudados, efectuar a comparação dos dados experimentais com as previsões teóricas dos modelos globais de potenciais α-nucleares. Permitirão também um estudo detalhado de "famílias" de potenciais locais com vista a melhorar os modelos de previsão teóricos e assim aprofundar o conhecimento na área da astrofísica.

Palavra-chave: p-process, supernova tipo II, dispersão elástica α, secção eficaz de interacção, potenciais α-nucleares.

Contents

List of Figures

List of Tables

Chapter 1

Introduction

The goal of this work was the measurement of the differential elastic scattering cross section of α particles from ^{64}Zn, ^{113}In and ^{115}In isotopes. The measured data will allow the extraction of the properties of the α-nuclear potential that enters into the modelling of the so-called p–process.

The measurements were performed using the cyclotron accelerator present at the nuclear physics laboratory at the ATOMKI institute in Debrecen, Hungary. Beams of α particles were accelerated at different energies (12.075 MeV, 16.137 MeV and 19.49 MeV), close to the Coulomb barrier of the considered isotopes. Complete angular distributions for the studied reactions were obtained.

The present Master Thesis focuses on the measurement, analysis and theoretical interpretation of the data obtained for the reaction ^{64}Zn(α,α)^{64}Zn at 12.075 and 16.137 MeV. Followed by a short introduction to the p–nuclei and the modeling of the astrophysical process in which these nuclei are produced (Section 1.1), and by an overview of the characteristics of nuclear reactions and in particular the elastic and Rutherford scattering (Chapter 2), the various aspects related to the experimental setup and the measurement of the angular distribution are presented (Chapter 3). The last part of this Thesis will concentrate on the theoretical analysis of the reactions ^{64}Zn(α,α)^{64}Zn (Chapter 4) and ^{113}In(α,α)^{113}In and ^{115}In(α,α)^{115}In (Chapter 5).

1.1 Heavy element nucleosynthesis

1.1.1 p-nuclei

The majority of elements are produced by stellar nucleosynthesis up to the iron peak, at this point the process of nuclear fusion that produces these elements no longer releases energy and the fusion reaction will therefore consume energy to produce heavier elements. As this is not energetically efficient the fusion reaction will eventually halt, creating an abundance peak around the iron elements.

The elements above the iron peak are thought to be produced via neutron capture reactions in s and r–processes [2]. The s–process is a slow neutron capture process, a nucleosynthesis process that occurs at low neutron density and intermediate temperatures conditions in stars (namely AGB - Asymptotic Giant Branch stars $\sim$ 0.6 to 10 solar masses). The r–process is a rapid neutron capture process, this process is thought to occur in core-collapse supernovae.

However, there is a set of 35 stable nuclei which cannot be produced by any neutron capture mechanism. These nuclei are the so-called p–nuclei. A list of these nuclei is presented in Table 1.1, together with their relative isotopic abundance.

The p-process of stellar nucleosynthesis aims to explain the production of the stable proton-rich nuclei heavier than iron that are observed in the solar system [2]. Several scenarios have been proposed to account for the bulk of p–nuclei abundances in the solar system, as well as for
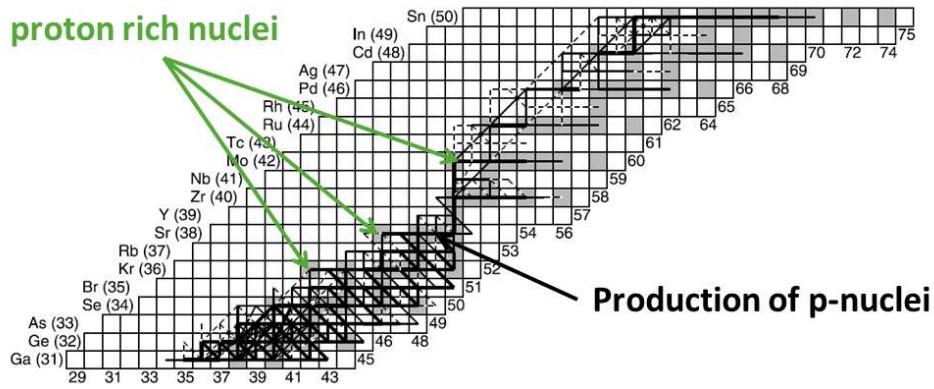
Figure 1.1: p-process reaction paths. Adapted from [1].

some deviations to the *p*-isotope composition of some elements discovered in primitive meteorites [3].

Among the several scenarios suggested for the production of *p*–nuclei, the photodisintegration of heavy nuclei produced by the *s* and *r*–process, the so called γ–process is a very strong candidate, and several articles have been devoted on this subject.

Table 1.1: List of all 35 *p*-nuclei. The relative isotopic abundances are taken from [4].

Nucleus	Isotopic abundance (%)	Nucleus	Isotopic abundance (%)
^{74}Se	0.88	^{132}Ba	0.10
^{78}Kr	0.34	^{138}La	0.09
^{84}Sr	0.56	^{136}Ce	0.19
^{92}Mo	14.84	^{138}Ce	0.25
^{94}Mo	9.25	^{144}Sm	3.10
^{96}Ru	5.52	^{152}Gd	0.20
^{98}Ru	1.88	^{156}Dy	0.06
^{102}Pd	1.02	^{158}Dy	0.10
^{106}Cd	1.25	^{162}Er	0.14
^{108}Cd	0.89	^{164}Er	1.61
^{113}In	4.3	^{168}Yb	0.13
^{112}Sn	0.97	^{174}Hf	0.16
^{114}Sn	0.66	^{180}Ta	0.01
^{115}Sn	0.34	^{180}W	0.13
^{120}Te	0.09	^{184}Os	0.02
^{124}Xe	0.12	^{190}Pt	0.01
^{126}Xe	0.11	^{196}Hg	0.15
^{130}Ba	0.11		

1.1.2 γ - process

The γ-process is thought to be responsible for the production of the p-nuclei (a series of 35 isotopes from ^{74}Se to ^{196}Hg) and occurs via the photodisintegration of stable seed nuclei present at the stellar plasma, at the very high temperatures characteristic of explosive burning. The sites for the occurrence of this process are thought to be the explosive burning at the O/Ne

layers in massive stars [3, 5, 6]. As the photodisintegration occurs, neutron, proton and α emission channels compete with each other and also with the β^+ decays further off the valley of stability. The sequence of photodisintegrations starts with a series of (γ, n) reactions, moving the nuclide abundances to the proton-rich side. The (γ, p) and/or (γ, α) reactions become dominant at some point of the isotopic chain, and this redirects the flow of mass to another chain. As the temperatures drop, photodisintegration becomes less effective, forcing the branch points to change, and the β^+ decay to become dominant. After a while, the photodisintegration stops entirely and the remaining nuclei decay back to the valley of stability. Looking at this general picture of the γ-process, it is clear that the branching are determined by the dominance of either the (γ, p) and/or (γ, α) over the (γ, n) reactions, and these branching are crucial to determine the radioactive progenitors of the stable p-nuclei. Other factors that influence the γ-process are the absolute values of the reaction rates, which determine the dynamics and the time-scales. The absolute values on the other hand, are also dependent on the time-dependent temperature profiles, characteristic of the chosen astrophysical scenario. The branching themselves only depend on the ratios of the reaction rates involved [6].

The simulated nuclear network of a γ-process can consist of more than 2000 isotopes and more than 20000 different reactions. It is technically impossible to measure the experimental cross sections of all reactions for all isotopes at all relevant astrophysical energies.

1.1.3 Hauser-Feshbach Statistical Model

Due to the huge number of reactions and isotopes involved in the γ-process, it is imperative to use a statistical model that can provide a realistic value for the necessary cross sections. The model used to achieve this is the Hauser-Feshbach statistical model [7], where the cross section $\sigma_{\alpha\gamma}^{\mu}$ for the reaction $i^{\mu}(\alpha, \gamma)l^{\nu}$, in which an α particle captured by a target nucleus i in a state μ, leaving the residual nucleus l and a photon is given by:

$$\sigma_{\alpha\gamma}^{\mu} = \frac{\lambda_{\alpha}^2}{4\pi} \frac{1}{(2J_i^{\mu}+1)} \sum_{J\pi}(2J+1)\frac{T_{\alpha}^{\mu}(J^{\pi})T_{\gamma}(J^{\pi})}{T_{tot}(J^{\pi})} \tag{1.1}$$

The variable λ_{α} is the wavelength of the system $\alpha + i$. The transmission coefficient $T_{\alpha}^{\mu}(J^{\pi})$ measures the probability of forming a compound nucleus in state J^{π}. Also, $T_{\gamma}(J^{\pi}) = \sum_{\nu} T_{\gamma}^{\nu}(J^{\pi})$ is the transmission coefficient for the decay of a compound nuclear state into the pair $l + \gamma$, considering all possible states ν of l that can be populated in the reaction. $T_{tot}(J^{\pi}) = \sum_{i,j} T_i^{\lambda}(J^{\pi})$ is the total transmission coefficient for the decay of the compound nuclear state into any combination of nucleus i and particles j that can be formed from all possible decay modes of λ.

Considering Eq. 1.1 it is possible to calculate the necessary cross sections. However the correct transmission coefficients must be known or estimated $(T_{\alpha}^{\mu}(J^{\pi}), T_{\gamma}(J^{\pi}), T_{tot}(J^{\pi}))$. To obtain these coefficients, an optical potential model $U(r)$ can be used to solve the Schrödinger equation and calculate the necessary values.

$$i\hbar\frac{\partial \psi}{\partial t} = \frac{-\hbar^2}{2m}\nabla^2\psi + U(r)\psi \tag{1.2}$$

The Schrödinger equation is depicted with the usual coefficients, $\hbar$ the Planck constant divided by 2π, the wave function ψ and mass m. For the elastic scattering case (see section 2.1, the Eq. 1.2 can be rewritten as:

$$E\psi(\vec{r}) = \left[-\frac{\hbar^2}{2\mu}\cdot\nabla^2 + U(r)\right]\psi(\vec{r}) \tag{1.3}$$

E is the energy of the stationary state, μ is the reduced mass of the system and ψ is the wave function. This wave function ψ is the sum of a plane and a spheric wave, and can be described

as follows:

$$\psi(\overrightarrow{r}) = A_0 \left(e^{i \cdot \overrightarrow{k} \cdot \overrightarrow{r}} + f(\theta, \phi) \frac{e^{ikr}}{r} \right) \tag{1.4}$$

$\overrightarrow{k}$ is the wave number of the incoming wave and $f(\theta, \phi)$ is the scattering amplitude. Integrating Eq. 1.4 over all degrees of freedom in the polar coordinate system, we obtain the square mean value of the wave function which relates to the density ρ of emitted particles:

$$\rho = \frac{A_0^2}{r^2} |f(\theta, \phi)|^2 \tag{1.5}$$

The differential cross section is defined as as the number of particles emitted per solid angle $d\Omega$ by the incident flux of particles per unit time, therefore from Eq. 1.5 the differential cross section $\frac{d\sigma}{d\Omega}$ can be extracted:

$$\frac{d\sigma}{d\Omega}(\theta, \phi) = |f(\theta, \phi)|^2 \tag{1.6}$$

Considering in the scattering effects both the nuclear and electromagnetic effects, the total scattering amplitude $f(\theta, \phi)$ can be written as:

$$f(\theta, \phi) = f_C(\theta) + f_N(\theta, \phi) \tag{1.7}$$

And as such, the differential cross section for the elastic scattering of a particle a in a target X is given by:

$$\frac{d\sigma}{d\Omega}(\theta, \phi) = |f_C(\theta) + f_N(\theta, \phi)|^2 \tag{1.8}$$

1.1.4 Optical Model

The *optical model* is a simplification, a treatment of the interaction between 2 particles in the presence of absorptive effects as an interaction potential, in this case an α particle and the target nucleus, a many-body problem which is reduced to a 2 body problem. It has such a name, because the calculation resembles that of incident light on a somewhat opaque glass sphere. The optical model $U(r)$ is normally defined in terms of a complex potential, such as:

$$U(r) = V_C(r) + V_N(r) \tag{1.9}$$

The components of the optical potential, are the Coulomb Potential $V_C(r)$ and a Complex Nuclear Potential $V_N(r)$. The Coulomb Potential $V_C(r)$ is described as:

$$V_C(r) = \begin{cases} Z_P Z_T e^2 \dfrac{3 - \left(\frac{r}{R_C}\right)}{2R_C} & for \ r \leq R_C \\ \dfrac{Z_P Z_T e^2}{r} & for \ r > R_C \end{cases} \tag{1.10}$$

The Coulomb Potential is considered the potential of an homogeneously charged sphere, with Z_P and Z_T the atomic numbers of the incident particle Z_P and the target Z_T, e is the elementary charge (1.602 $\times 10^{-19}$ C) and R_C is the radius of the sphere.

The Complex Nuclear Potential has an real $V(r)$ and imaginary $W(r)$ part:

$$V_N(r) = V(r) + iW(r) \tag{1.11}$$

The parameterizations for the Complex Nuclear Potential $V_N(r)$ can vary, but the most commonly used are the Wood-Saxon parameterizations:

$$V(r) = V_0 \; f_{V,R}(r) \tag{1.12}$$

$$W(r) = W_V \; f_{V,I}(r) - 4 \; a_{S,I} \; W_S \frac{df_{S,I}(r)}{dr} \tag{1.13}$$

$$with \quad f_{i,j} = \left(1 + exp\left(\frac{r - R_{i,j}}{a_{i,j}}\right)\right)^{-1} \; i = V, S \; and \; j = R, I$$

The parameters of the optical potential model, V_0 the depth of the real nuclear volume potential, W_V the depth of the imaginary volume potential, W_S the depth of the imaginary surface potential, $a_{V,R}, a_{V,I}, a_{S,I}$ are the diffusenesses of each considered potentials. The $f_{i,j}$ are the Woods-Saxon parameterizations, i can be V or S to indicate if it is a Volume or Surface potential and j can be R or I to indicate if it is a Real or Imaginary part of the nuclear potential.

These parameters can be extracted from α scattering experiments using appropriate fitting of the experimental data. As such that constitutes the primary motivation to the realization of these scattering experiments.

1.1.5 Cross Section

The concept of a cross section describes the probability of interaction of particles with other particles and/or light (radiation). In the case of this experiment, the cross section describes the probability of occurrence of elastic α-scattering (section 2.1) in targets of ^{64}Zn, ^{113}In and ^{115}In.

As described in the previous section, the parameters of the optical potential model can be extracted from α scattering experiments. However to obtain the cross section a nuclear reaction program is necessary, in order to perform the complex and morose calculations involving the solving of the Schrödinger equation (Eq. 1.2).

The program "a0", is a nuclear reaction program designed to calculate cross sections, perform χ^2 analysis of experimental data, it is able to use several different potentials and parameterizations.

The optical model $U(r)$ is fed to the program "a0" [8], this program calculates the Scattering S Matrix for the chosen nuclear potential, the matrix is calculated only with the elastic scattering terms taken into account. The code also considers a sufficient amount of partial waves. After performing these operations the code returns the corresponding cross section, in our case the differential cross section for the specified optical potential.

In sum, by obtaining a precise angular distribution of the cross section, one can constrain the optical potential parameters, and use the obtained potential to solve the Schrödinger equation, which in turn gives the transmission coefficients necessary for the Hauser-Feshbach statistical model. The predictions of the Hauser-Feshbach model can then be used to estimate the reaction rates along a nuclear network, allowing the estimation of the abundances of the nuclear isotopes.

Chapter 2

Scattering Theory

2.1 Elastic α scattering
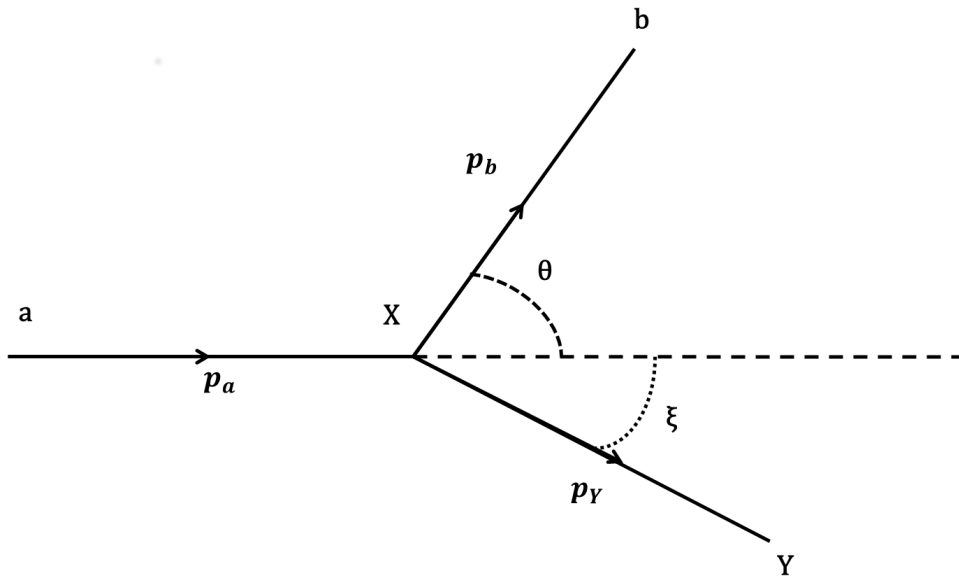
Figure 2.1: Basic Reaction Geometry for $a + X \rightarrow b + Y$

A typical nuclear reaction can be written as $a + X \rightarrow b + Y$, where a is the incoming particle, X the target, and b and Y the reaction products. A more compact way to refer to this is $X(a, b)Y$. In the case of *elastic* α scattering, a and b are the same α particle, X is the target nucleus, and at the end of the reaction $X = Y$, remaining in its ground state. If there is exchange of energy between the particles, enough to promote the target X to an excited state, then it's called an *inelastic* collision.

Taking in account the schematics presented by Figure 2.1, the following set of equations for the conservation of linear momentum can be easily obtained [9].

$$p_a = p_b \cos(\theta) + p_Y \cos(\xi) \tag{2.1}$$

$$0 = p_b \sin(\theta) - p_Y \sin(\xi) \tag{2.2}$$

p_a, p_b and p_Y are the linear momentum of particles a, b and Y, θ is the angle in relation to the incoming direction at which particle b is scattered, ξ is the angle at which particle Y is scattered. To solve this set of equations we must also note that $Q = T_Y + T_b - T_X - T_a$, i.e., the

reaction Q value is the difference between the final and initial kinetic energies, $T_{final} = T_Y + T_b$ and $T_{initial} = T_X + T_a$.

It is then possible to determine the final equation that relates the kinetic energy of particle b, T_b with angle θ:

$$T_b^{1/2} = \frac{(m_a m_b T_a)^{1/2} \cos(\theta) \pm \left\{ m_a m_b T_a \cos^2(\theta) - (m_Y + m_b)[T_a(m_a - m_Y) - m_Y Q] \right\}^{1/2}}{m_Y + m_b} \quad (2.3)$$

For elastic scattering we have that $a = b$, so they have the same mass ($m_a = m_b$), also $X = Y$, thus $m_X = m_Y$ and $Q = 0$, therefore we can simplify Eq. 2.3, and obtain:

$$T_b^{1/2} = T_a^{1/2} \frac{m_a \cos(\theta) \pm \left\{ m_a^2 \cos^2(\theta) - (m_X^2 - m_a^2) \right\}^{1/2}}{m_X + m_a} \quad (2.4)$$

Eq. 2.4 allows the calculation of the expected value of the kinetic energy T_b of particle b, in this case the α particle deflected by the target X, for a determined angle θ and α beam kinetic energy T_a. This equation provides a useful feature for the calibration of the detectors.

2.2 Rutherford scattering
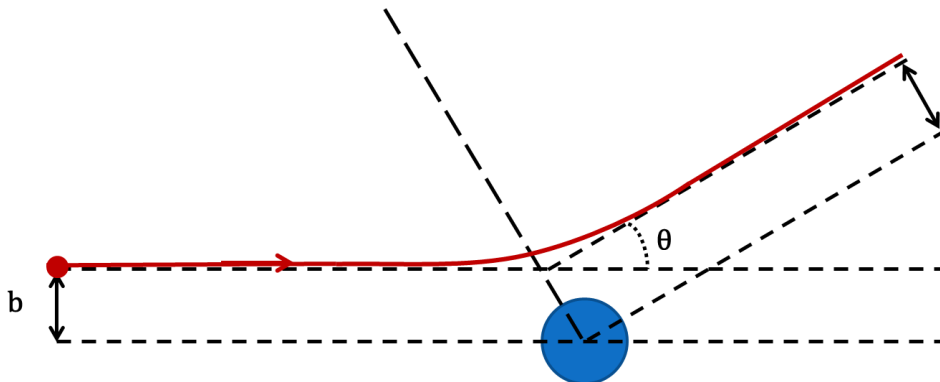
Figure 2.2: Rutherford Scattering Scheme

In the previous section, the description of a pure kinematic collision between particles was presented. However, the charge of the particles was not taken into account. As it is well known, the nucleus has a distribution of electric charge, which can be studied by the electric (Coulomb) scattering of a beam of charged particles. This scattering is also called *Rutherford Scattering* and its schematics can be seen in Figure 2.2. Since the Coulomb Force is a $\frac{1}{r^2}$ force, the scattered particle follows a hyperbolic path (also assuming the target particle fixed). As the particle follows a straight path, that would pass a distance b from the nucleus if there were not repulsive force between the two particles, b is called the *impact parameter*. However, the particle thus indeed feel a repulsive force and is scattered with angle θ. Now if we take into account the balance of energy, before and after the scattering, we can assume that far from the nucleus, the incident particle doesn't feel any force, and so has negligible potential energy, and thus it only has kinetic energy $T_a = \frac{1}{2} m v_0^2$. The angular momentum relative to the target nucleus is $|\overrightarrow{r} \times m \overrightarrow{v}| = m v_0 b$ at large distances. When passing close to the target nucleus, the particle reaches a minimum distance of separation r_{min} (dependant on b), which has its minimum value for $b = 0$, the head-on collision, in which the particles comes to an momentary rest, before reversing its motion.

The *Rutherford Scattering* is cylindrically symmetric about the beam axis, and as such the particles with impact parameter $b + db$ are scattered into a ring at angles $\theta + d\theta$.

The integration of the contribution of all rings and other considerations (see [9]) we can obtain the final equation that describes the differential cross section for Rutherford scattering.

$$\frac{d\sigma}{d\Omega} = \left(\frac{zZe^2}{4\pi\epsilon_0}\right)^2 \left(\frac{1}{4T_a}\right)^2 \frac{1}{\sin^4\frac{\theta}{2}} \tag{2.5}$$

2.3 Frame of reference

In our experiment we perform the measurements in the laboratory frame of reference, however it is necessary to convert the measurements in this reference frame to the center of mass frame. To achieve this we use the following equation:

$$\theta_{C.M.} = \theta_{lab} + arcsen\left(\frac{m_{proj}}{m_{target}} \times sen(\theta_{lab})\right) \tag{2.6}$$

The center of mass frame of reference angle $\theta_{C.M.}$ is calculated with the lab angle θ_{lab}, m_{proj} ís the mass of the projectile and m_{target} the mass of the target.

Chapter 3

The ^{64}Zn$(\alpha,\alpha)^{64}$Zn Experiment

The α particle scattering experiment was performed in the fall of 2011 and lasted about 10 days, at the ATOMKI Lab, in Debrecen, Hungary. During the whole beam time the reactions studied where the elastic scattering processes ^{64}Zn$(\alpha,\alpha)^{64}$Zn, ^{113}In$(\alpha,\alpha)^{113}$In and ^{115}In$(\alpha,\alpha)^{115}$In.

In the following sections the various aspects related to the measurements, from the production of the accelerated α-particle beam to the analysis of the measured spectra, will be presented.

3.1 Experimental Setup

The experimental setup for this experiment requires specialized instrumentation such as a cyclotron (MGC-20E) to accelerate α particles at different energies and a scattering chamber specially designed and built to measure the angular distribution of the elastically scattered α particles. In Fig. 3.1 a schematic view of the ATOMKI laboratory can be observed, depicting the entire beam line, from the Cyclotron to the scattering chamber.

Cyclotron MGC-20E

Bending Magnet

Scattering Chamber
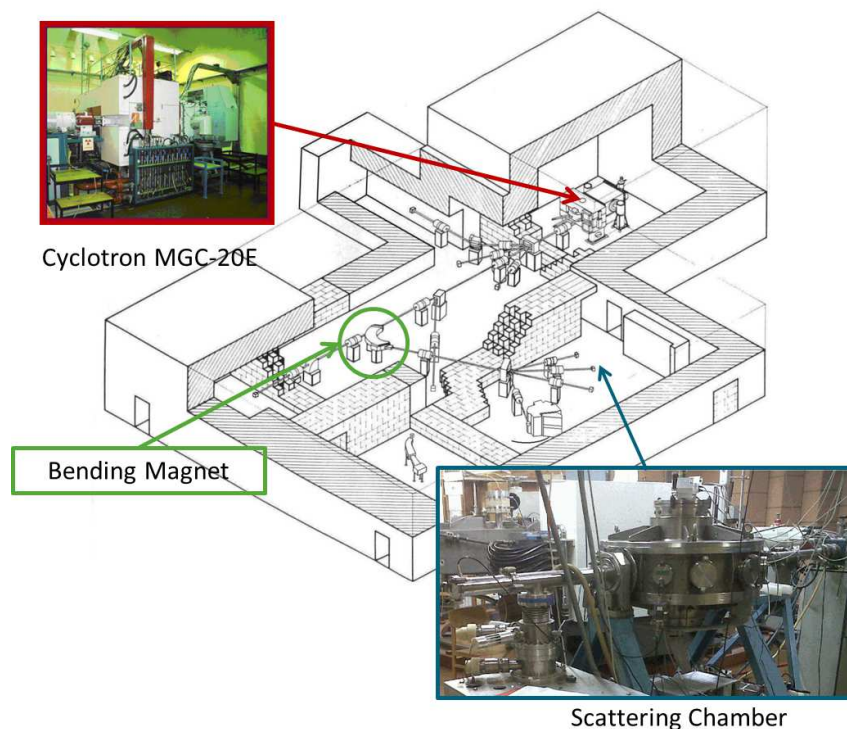
Figure 3.1: Artistic view of the cyclotron laboratory at ATOMKI

3.1.1 Cyclotron

The cyclotron present at the ATOMKI institute allows for the acceleration of charged particles (protons, deuterons, $^3\text{He}^{++}$ and α), for a variety of applications and fundamental research experiments. In the case of α particles, it provides beam energies between 2 and 20 MeV, with an energy spread of $\frac{\delta E}{E} < 10^{-3}$, and a beam intensity at the exit of the cyclotron of approximately 20 μA. A bending magnet placed in the beam line allows for the selection of the particle energies, and the manipulation of the beam characteristics, such as beam width and intensity. In this experiment the cyclotron supplied 3 different beam energies, 12.075 MeV (^{64}Zn), 16.137 MeV (^{64}Zn,

Figure 3.2: Cyclotron MGC-20E

^{113}In, ^{115}In) and 19.49 MeV (^{113}In,^{115}In) with beam intensity at the target of the order of 200 nA. [10]

3.1.2 Scattering Chamber

The Scattering Chamber is one of the most vital elements of the experiment. It provides the necessary vacuum conditions (about 10^{-5} mbar) to avoid the absorption/attenuation of the α particles by the atmospheric air. The chamber, with an inner diameter of 78.8 cm, contains 2 turntables on which it is possible to mount up to 10 detectors, 5 on each turntable, and the associated mechanics to move them around allowing a coverage of almost the full angular range. In addition, two detectors were placed at forward angles ($15°$) to monitor the experiment and to normalize the measured cross-section.

At the center of the chamber, a target holder with the various targets used during the experiment (see Section 3.1.2) was placed. It allows for the automatic change of the target under study and the rotation of the samples with respect to the incident beam. In addition to the targets considered for the measurement of the angular distributions, the holder also hosted 2 "slits" (metal plates with rectangular holes), which were used to optimize and calibrate the width of the beam. The first slit had a 6×6 mm^2 area. Initially, the α-beam was tuned and focused at the target position using this slit by measuring the current deposited on the frame. This procedure continued until less than 1% of the total beam current was measured on this aperture. To further collimate the beam, the process was repeated for a second slit with 6×2 mm^2, thus assuring a well defined beam spot throughout the entire experiment. This is crucial for a precise determination of the scattering angle [11]. The chamber, as it can be observed in Figure 3.1 is located in one of the beam lines of the cyclotron after the bending magnet, situated in an adjacent room to the cyclotron. All working lines and rooms are situated in an section of the building with radiation shielding and restricted access.

In Figure 3.3a a diagram of the interior of the scattering chamber is shown, where the 2 turntables are represented, the mounting points for the detectors, at the center of the chamber the target system, the beam entrance, the monitor detectors and the "*Faraday Cup*" for charge collection. A view of the scattering chamber from outside is shown in Fig. 3.3b.

The signals from the movable detectors are sent by cables connected to an interface at the bottom of the scattering chamber, this interface allows connection at the exterior of the chamber to the amplification system.
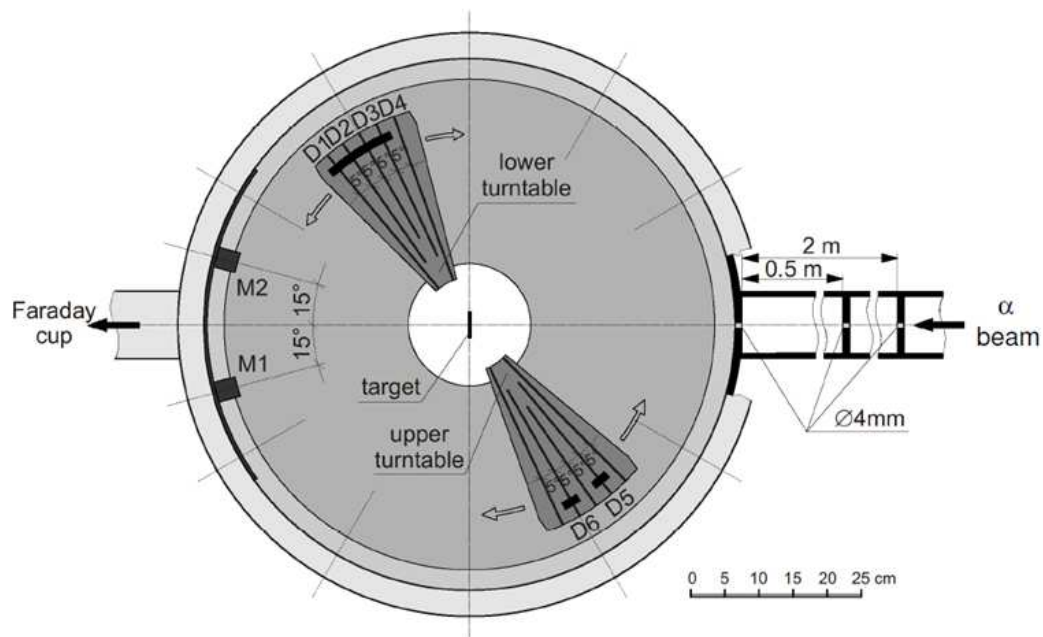
(a) Diagram of the Scattering Chamber

(b) External view of the Scattering Chamber

Figure 3.3: On the upper figure a diagram of the scattering chamber (taken from [12]) is shown. The α particle beam enters the chamber from the right side. The two turntables holding the detectors used to measure the elastically scattered α particles are shown, together with the monitor detectors located at 15° with respect to the axis defined by the incident beam. During the present experiment the lower turntable hosted 5 detectors, while on the upper one just 2 detectors were placed. The lower figure shows a view from outside the scattering chamber. In addition to the vacuum system located under the chamber, it is possible to observe the Faraday cup located at the left side of the picture, on which the current of the unreacted beam was measured.

Targets

During the experiment described in this work, several targets were used for the measurement of the angular distribution of the elastically scattered α particles and for angular calibration purposes. All targets were placed in the target holder described in the previous section prior the start of the experimental campaign. During the experiment, it was possible to choose the target to be studied without having to break the vacuum inside the chamber.

The targets were prepared at the ATOMKI target laboratory using the evaporation technique. Highly enriched isotopic material was used to manufacture the targets by evaporating it to a very thin ^{12}C foil ($\sim 40 \ \mu g/cm^2$). A very high isotopic enrichment is necessary in order to be sure that the elastic (and inelastic) scattering peaks that we observe are mainly from the element in study and not from one of the other isotopes of that element, as that would introduce an error in the calculation of the cross section, and therefore jeopardize the subsequent analysis.

A total of four targets were produced, using a Leybold UNIVEX 350 vacuum evaporator [13], two targets for the ^{64}Zn, and one target each for the ^{113}In and ^{115}In elements, each one with a thickness of $\sim 100 \mu g/cm^2$). A quick calculation using program SRIM [14], shows that at the worst case scenario the loss of beam energy in the ^{64}Zn layer and the ^{12}C layer is ~ 40 keV for the incident beam energy of 12.075 MeV, which is less than the resolution of the detectors used in this experiment.

Detectors

As shown in the description of the scattering chamber, a total of 9 detectors were used during the measurement of the elastic scattering cross section reactions on ^{64}Zn, ^{113}In and ^{115}In. The seven detectors located on the turntables were silicon barrier detectors of type ORTEC ULTRA BU-013-050-500 [15]. These detectors provide an energy resolution of 13 keV/channel at 5,486 MeV (α from ^{241}Am), with an active area of 50 mm^2 and a depletion zone of 500 μm. With these detectors almost the full angular range, between 20° to 175°, of the elastic scattering process was covered. The solid angle of each movable detector is of the order of $\Delta \Omega \approx 1.0 \times 10^{-4} sr$. Regarding the two remaining detectors, the so-called "monitor detectors", they have the same characteristics as the 7 movable detectors used for the angular distribution measurements, but with a different holder. The monitor detectors were fixed at an angle $\pm$ 15° with respect the incident beam axis with a solid angle of $\Delta \Omega = 8.2 \times 10^{-6} sr$.

The data measured by the monitor detectors is used to normalize the data obtained by each of the other detectors. Doing this, it is possible to eliminate (or at least minimize) systematic uncertainties, such as the effects of irregular target thickness or those related to the measurement of the intensity of the beam on target. As the monitor detectors are at very forward angles and taking into account the energies considered for the performed measurements, it's possible to assume that the observed yield is purely due to Rutherford scattering.

Spectroscopic Amplifier CAEN MOD. N568B/LC

The CAEN MOD. N568B/LC Amplifier board provides an amplification system for several detectors, up to a maximum of 16. It allows the control of several parameters associated to the measurement of the electrical signals induced by the charged particles in the detectors, such as pole-zero correction (PZ), shaping time, amplification gain and output inversion. The board is controlled by an onboard PC board, in this case the A1303 H. S. CAENET PC Controller (PCI bus), using a H.S. CAENET cable. The software to control the board was the CAENHVOP OPC Server, providing a graphic interface to control the different considered parameters [16].
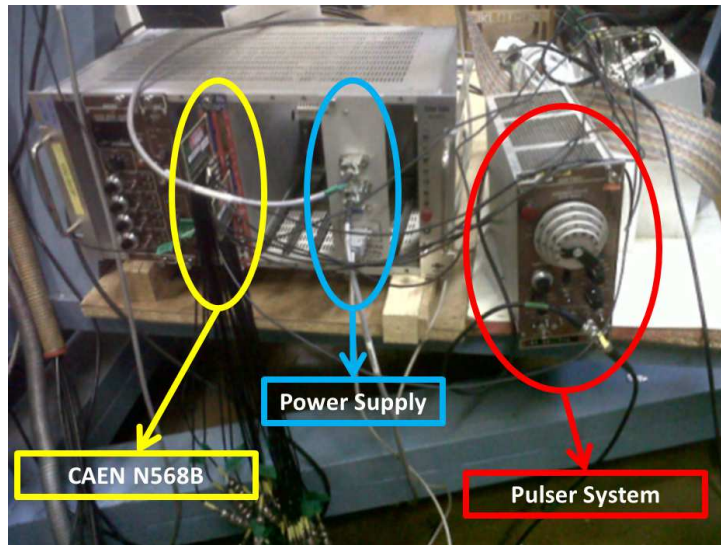
Figure 3.4: View of the electronics used during the experiment. The CAEN Spectroscopic Amplifier System (left) and the power supply for the detectors (center) inserted in the NIM Crate used for the experiment are shown, together with the ORTEC Pulser System (right).

Pulse Generator

The Pulse Generator was used during the experiment to determine the dead time in each of the detectors. An ORTEC Research Pulser provided electrical impulses to all the detectors, at an amplitude equivalent to an energy of ≈ 24 MeV.

On the pulser output a derivation was placed to split the pulser signal in two (see Figure 3.4), sending separately the pulser signal to the lower and upper turntables. By separating the signal for both backward and forward angles it was possible to have a more detailed control on the pulser signal for both branches. Some of the electronics used can be seen in Figure 3.4, showing the main connections of the amplification board CAEN MOD. N568B/LC, mounted in a NIM Crate, and the ORTEC Pulser System.

The output signals from the amplification board were connected to a switch panel, which allowed the further treatment of the signals outside the experimental hall in which the scattering chamber is placed. In this way, the controlling hardware and software could be placed outside the experimental hall, protecting them from harmful radiation, and also protecting the associated personnel controlling the experiment.

3.2 Data Acquisition and Measured Spectra

The signals from the detectors were fed to five different ORTEC ASPEC-927 Dual 16k Multichannel modules [17]. These modules were connected to the data acquisition computer via USB ports, in which the acquisition was performed using the commercial software MAESTRO for Windows Model A65-B32 Version 6.06, which manages and stores each of the spectra from each detector. Each spectrum has a memory-size of 2048 channels. To correlate the channel number to the α particle energy, it is necessary to calibrate the detectors, in order to obtain an channel-energy equation and so extract the respective energy for a determinate channel. (View section 3.3.1).

The measurement of a complete angular distribution was planned considering two main angular ranges, in order to obtain the maximum information in the available time for the experiment:

- Forward: between $20°$ to $100°$, in which measurements were performed with $1°$ steps.

- Backward: from $100°$ to $175°$, with measurements performed in $2.5°$ steps.

The ^{64}Zn target was initially irradiated with an α particle beam of E = 12.075 MeV. The whole angular range was covered by 48 different settings of the detectors. A total of 16 hours and 15 minutes of target irradiation were employed at this energy to measure the whole angular distribution.

After changing the beam energy to 16.137 MeV, three angular distributions were measured for the elastic scattering reactions on ^{64}Zn, ^{113}In and ^{115}In. As for the case of ^{64}Zn, 58 different angular settings were executed, resulting in a total of 21 hours and 30 minutes of target irradiation. Similar measurements were performed for the Indium isotopes. The details of these measurements are not in the scope of the present work. The theoretical analysis of the elastic scattering reactions on ^{113}In and on ^{115}In at this energy and at 19.49 MeV is described in Chapter 5.

3.2.1 Forward Angles

The measurement at forward angles profits from the high count rate of the reaction under study, allowing a complete coverage of the forward angular range with very low statistical errors. For each measurement a region of interest (ROI) was considered for the elastic peak, under which a minimum of 6000 events was requested to start a new measurement at a different angular position. In this way, it was possible to limit the statistical error to be below $\approx 1.3\%$ across all forward angles. Typical spectra obtained in the forward angle region are shown in Fig. 3.5 and Fig. 3.6.

Forward angles at 12 MeV
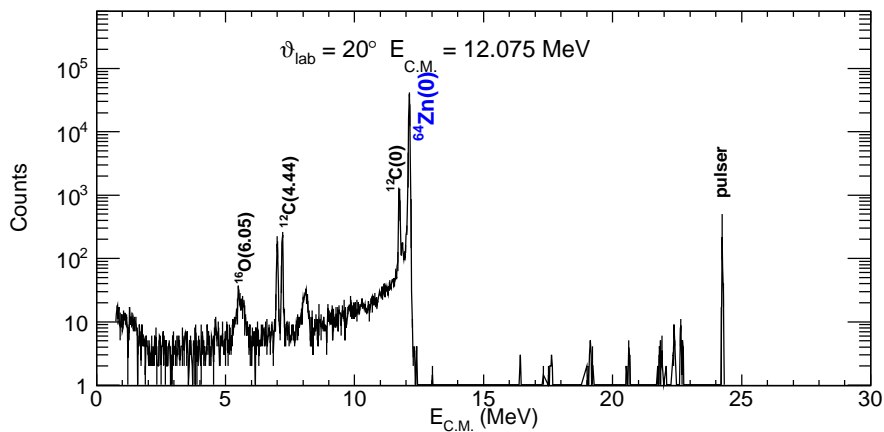
Figure 3.5: Spectrum from the reaction ^{64}Zn$(\alpha, \alpha)^{64}$Zn at E = 12.075 MeV under $20°$.

Forward angles at 16 MeV
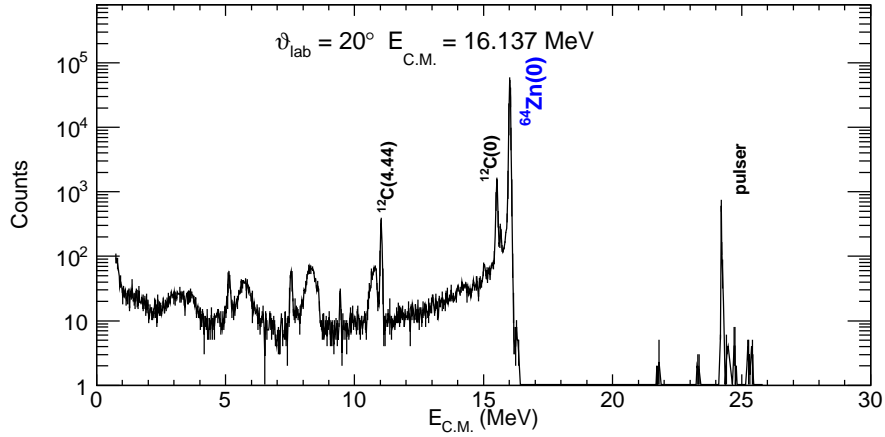
Figure 3.6: Spectrum from the reaction $^{64}\text{Zn}(\alpha, \alpha)^{64}\text{Zn}$ at E = 16.137 MeV under 20°.

3.2.2 Backward Angles

In contrast with the relatively faster coverage of the forward angle region, the low count rate at backward angles turns the measurements more time consuming. It's necessary to account for long irradiation times in order to have a meaningful statistic. In this case, a lower limit of 1000 measured reaction events in the ROI of the elastic scattering peak was set for every measured angular position. This corresponds to a maximum statistical error of $\approx 3.2\%$. Typical spectra obtained in the backward angle region are shown in Fig. 3.7 and Fig. 3.8.

Backward angles at 12 MeV
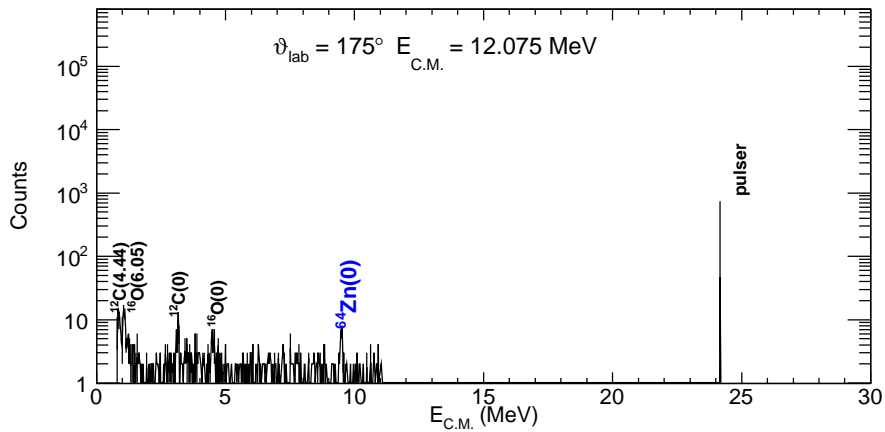
Figure 3.7: Spectrum from the reaction $^{64}\text{Zn}(\alpha, \alpha)^{64}\text{Zn}$ at E = 12.075 MeV under 175°.

Backward angles at 16 MeV
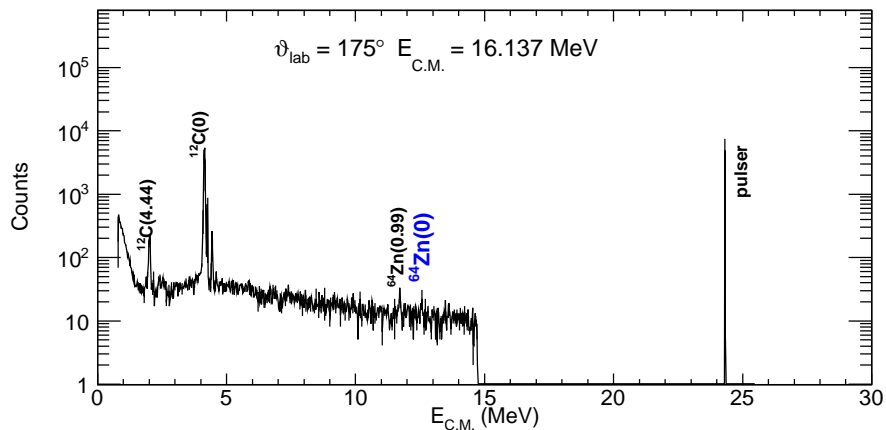
Figure 3.8: Spectrum from the reaction ^{64}Zn$(\alpha, \alpha)^{64}$Zn at E = 16.137 MeV under 175°.

In order to optimize the use of the beam time, the detectors of the upper turntable (see Fig. 3.3a) were kept at a fixed backward angle while the detectors on the other plate covered the forward angular range. Therefore several "Runs" were performed in which the upper turntable was fixed to increasing the necessary statistics, while moving the lower turntable.

As for the analysis, this means that the spectra of the backward angles needs to be accumulated, and the corresponding monitor detector spectra also needs to be analysed in a similar way, in order to achieve the correct normalization. In addition the spectra obtained by the monitor detectors for each of those runs was also individually analysed, as it was needed for forward angle normalization, and the results of the sum of analyses of individual spectrum is the same as the analysis of the sum of spectra.

3.3 Calibrations

During the experiment it was necessary to perform several calibrations. I shall discuss two of the most important, the detector energy calibration and the angular calibration.

3.3.1 Energy Calibration

The detector energy calibration is performed by using Eq. 2.4 for the most forward angle of the considered detector and then relating the peak centroids to the respective energy. To improve this calibration, in addition to the elastic peak, several inelastic peak energies are also considered, thus providing more data points.

The channel-to-energy coefficients obtained are listed in Table 3.1. They are obtained after applying a linear fit $E = A \times Channel + B$ to the data points from Table A.1, E is the Energy of the peak and *Channel* is the channel number, A and B are the correspondent coefficients.

Detector	A (MeV/Channel)	B (MeV)
D1	1.46×10^{-2}	0.80
D2	1.74×10^{-2}	0.39
D3	1.60×10^{-2}	0.32
D4	1.49×10^{-2}	1.28
D5	1.56×10^{-2}	0.50
D6	1.52×10^{-2}	0.50
D7	1.63×10^{-2}	0.16
M1	1.28×10^{-2}	0.01
M2	1.42×10^{-2}	0.24

Table 3.1: Energy Calibration Coefficients (from 16MeV experiment).

For all cases, the curve fitted the data points with an deviation of less than 1% ($R^2 > 0.99$).

3.3.2 Angular Calibration

The angular calibration is a very critical calibration, since a small deviation of the expected angle can have drastic variations on the expected cross section, as can be seen in Eq. 2.5 for the Rutherford Scattering. This deviation is due to the fact that the detectors are mounted in the rails of a movable turntable (as can be seen in the Fig. 3.3a), the detector has a support that fits in the rail, however there is always some leeway, no matter how tight the fit between rail and support, therefore the alignment of each detector is not completely parallel to the rails, this causes a deviation in the angle of detection, that must be taken into account. The turntables themselves were calibrated pre-experiment in order to make sure they are at the correct angle, however during the operation of electro-mechanic instruments, these are bound to misalign due to repeated use. To prevent that, a remote visualization system was also present, i.e., there were cameras facing the angular indicator of each turntable in order to confirm the angle of each turntable at every moment, if some deviation occurred, this was corrected by manually overriding the values of the angular position in the turntables control program and then resetting the turntable to the correct position.

To perform this calibration we take advantage of the kinematics of the reaction $^{12}C(\alpha, \alpha)^{12}C$, by using a ^{12}C foil as a target. Fixing one detector at a certain angle, moving another detector around the recoil angle, we performed a coincidence measurement of both ^{12}C and α-particle. Kinematic calculations performed using the code LISE++ [18] for an α particle being dispersed at $60.00°$, show that we can expect a ^{12}C particle being ejected at $51.58°$.

In order to make sure we are in fact seeing a coincidence detection of a ^{12}C and α-particle, for each considered detector pair (see Fig. A.1 and Fig. A.2), the signals at the ADC of each

detector were gated between them, i.e., when a detector detects a charged particle it sends a signal to the pre-amplifier, which sends it to the amplifier and then to the ADC that transforms it in a signal a program in the PC can understand, these ADC also have the capacity to select desired results, such as only sending a signal to the computer if another ADC to which they are connected, has also detected a signal within a certain time-window, to ensure that they are in fact detecting the fragments of the same reaction.

In our case one of the detectors was positioned to detect the α-particles at the angle of $60.00°$, while another detector covered an angular region near the expected recoil angle of ^{12}C at $51.58°$, the ADC of each detector were gated, in order to ensure that only the results from the $^{12}C(\alpha, \alpha)^{12}C$ reaction are detected.

The results of the several coincidence measurement performed by the different detector pairs, can be seen in Fig. A.1 and Fig. A.2. A Gaussian fit was also performed for each data set, and the yield was normalized to the maximum value of the Gaussian function. This procedure allows us to compare the relative yield of each detector-pair in an equal manner. Also present in each sub-figure is the expected value of $51.58°$, represented by a grey area.
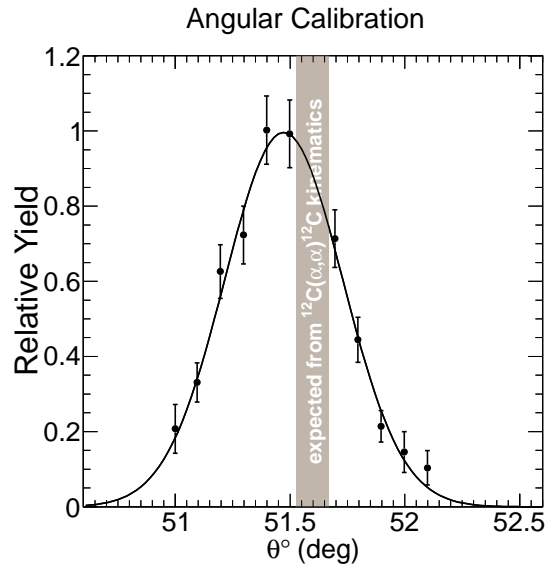
Figure 3.9: Angular Calibration for detector pair D2-D6. The grey area shows the expected angle of the scattered ^{12}C.

Following the Gaussian fit analysis of each detector-pair it is possible to extract the largest deviation from the expected value. The value was obtained from the D2-D6 pair in Fig. 3.9, since the maximum of the Gaussian function is present at $51.48°$, therefore the standard deviation from the expected result is $\Delta\theta = 0.10°$. To get an idea of the impact of this deviation, a quick calculation shows that the angular deviation of $\Delta\theta = 0.10°$ causes at worst an error of $\sim 2\%$ in the estimation of the cross section at $20°$ and at best an error $\sim 0.02\%$ at $175°$.

Chapter 4

^{64}Zn$(\alpha, \alpha)^{64}$Zn Data Analysis

The data obtained in the experiment, about 1000 spectra for the detectors and the monitor detectors were used in the analysis of the angular distribution between the range of 25° and 175° angle. In each spectrum the elastic α peak was analysed, since its peak area integration is the observable needed for the determination of the experimental elastic cross section. The equation that describes this is:

$$\left(\frac{d\sigma}{d\Omega}\right)(\vartheta) = \frac{N(\vartheta)}{N_{proj} \ N_{target}/F_T \ \Delta\Omega} \tag{4.1}$$

$N(\vartheta)$ represents the number of elastic scattered α particles at the angle ϑ in the laboratory frame. The number of incoming α particles is denoted by N_{proj}, whereas N_{target}/F_T is the total number of target atoms per unit area. The solid angle covered by the detector is symbolized by $\Delta\Omega$.

In order to accommodate and organize the enormous amount of data obtained during this experiment, and also to start the analysis of the spectra obtained, it was necessary to convert the data into ROOT CERN [19] data type. This data type allows the use of the ROOT CERN analysis tool kit, which includes, histogram building, histogram analysis, peak search, peak fitting, among other utilities.

The first step was to create a program to read each of the MAESTRO data files, which specifies the detector ID, the counts by channel, counting time, dead time, and the date and time at which the experiment was performed.

The data read by the analysis program is then stored into a three-dimensional matrix system that relates the "Run" number with the detector and each of the individual channels of each spectra. Having done that, it is possible for ROOT to read the matrix and recreate the histograms as seen in the MAESTRO program. Further analysis of the histogram is now possible, as it is now a ROOT object, and it is possible to use the channel-to-energy calibrations to renormalize the histogram and present the measured events as a function of energy.

4.1 ^{64}Zn$(\alpha, \alpha)^{64}$Zn Data Analysis

The data stored in the ROOT object created by the analysis program calibrated the spectra and rescaled from counts by channel to counts per energy, by using the channel-to-energy calibrations of subsection 3.3.1 for each detector.

After performing the normalization, an additional ROOT program was used to create the new normalized histograms. During the execution of this program, one of it subroutines marked the most significant peaks found in each spectrum for further analysis.

4.1.1 Peak Analysis

The peaks marked by the program were selected for analysis. This was performed by a systematic peak selection and subsequent peak area calculation. For each run the elastic peak was selected, the interval of channels selected was different for each detector, due to intrinsic factors. The peak area was calculated and stored for posterior use.

4.1.2 Peak Normalization

The normalization of the peak areas is crucial point in the analysis. Considering the monitor detector peak areas as a reference, the areas of each detector (D1 to D7) were normalized to the monitor detector peak areas of each run. As such the errors due to target imperfections and or beam instability are minimised [20]. Starting from Eq. 4.1, by noting that the monitor detectors are at ϑ_{Mon}, if we apply the equation for it's case and then use that result to normalize the general data from all the detectors, we can obtain the following equation:

$$\frac{\left(\frac{d\sigma}{d\Omega}\right)(\vartheta)}{\left(\frac{d\sigma}{d\Omega}\right)(\vartheta_{mon})} = \frac{N(\vartheta)\ \Delta\Omega_{mon}}{N(\vartheta_{mon})\ \Delta\Omega_{det}} \tag{4.2}$$

As it can be noted, the factors N_{proj}, the number of incoming α particles and N_{target}/F_T, the total number of target atoms per unit area, which are fixed quantities for each measurement, cancel in the resulting equation, minimizing the error of the overall measurement by eliminating the need to measure and/or estimate these quantities.

4.1.3 Rutherford Normalization

Departing from Eq. 4.2 we can express the $\left(\frac{d\theta}{d\Omega}\right)(\vartheta)$ as follows:

$$\left(\frac{d\sigma}{d\Omega}\right)(\vartheta) = \frac{N(\vartheta)\ \Delta\Omega_{mon}}{N(\vartheta_{mon})\ \Delta\Omega_{det}}\ \left(\frac{d\sigma}{d\Omega}\right)(\vartheta_{mon}) \tag{4.3}$$

However, as we assumed that the cross section at ϑ_{mon} is Rutherford, we can replace the differential cross section at ϑ_{mon} ($\left(\frac{d\theta}{d\Omega}\right)(\vartheta_{mon})$) with Eq. 2.5, obtaining as a result:

$$\left(\frac{d\sigma}{d\Omega}\right)(\vartheta) = \frac{N(\vartheta)\ \Delta\Omega_{mon}}{N(\vartheta_{mon})\ \Delta\Omega_{det}}\ \left(\frac{zZe^2}{4\pi\epsilon_0}\right)^2 \left(\frac{1}{4T_a}\right)^2 \frac{1}{\sin^4\left(\frac{\vartheta_{mon}}{2}\right)} \tag{4.4}$$

In order to apply the final normalization, we divide both sides of Eq. 4.4 with both sides of the general Rutherford Equation (2.5) and obtain the final normalization equation:

$$\frac{\left(\frac{d\sigma}{d\Omega}\right)(\vartheta)}{\left(\frac{d\sigma}{d\Omega}\right)_{Ruth}(\vartheta)} = \frac{N(\vartheta)\ \Delta\Omega_{mon}}{N(\vartheta_{mon})\ \Delta\Omega_{det}} \frac{\sin^4\left(\frac{\theta}{2}\right)}{\sin^4\left(\frac{\vartheta_{mon}}{2}\right)} \tag{4.5}$$

By performing these normalizations, we can remove the electromagnetic effect on the cross section and extract the information of the nuclear part of the cross section, observing it's effect across the entire angular distribution.

4.2 ^{64}Zn$(\alpha,\alpha)^{64}$Zn Global α nuclear potential analysis

A global α–nucleus potential is a model in which its parameters allow the calculation of the elastic α scattering cross section for a wide range of masses and energies.

The parameters for the global α–nucleus potential are derived from various fits to a wide array of experimental cross section data. However due several constraints, from insufficient/nonexistant experimental data from some isotopes, to different energies ranges at which the cross sections for some elements are available, also due to the different "behaviour" between light and heavy mass regions, and other factors, a truly global α–nucleus potential is as yet to be achieved. Nevertheless, some global α–nucleus potentials models do provide a very close description of the experimental data at given energies, and in the case of this work we considered some of the most used in this line of investigation: L. McFadden and G. R. Satchler [21], M. Avrigeanu *et al.* [22] and TALYS [23].

The McFadden potential [21] is an optical model potential that uses Woods-Saxon parameterizations for the real and imaginary volume parts while neglecting the imaginary surface potential. This model has only 4 parameters, $V0$, W_V, with $R_{V,R} = R_{V,I}$ and $a_{V,R} = a_{V,I}$. It was developed in 1965 for α particle elastic scattering on a wide array of elements, at energies of about 24.7 MeV, however despite it's simplistic formulation, it has been found to be reasonably accurate for a very wide range of nuclei and energies (from O to U).

The potential from Avrigeanu [22] is a standard optical model potential with Woods-Saxon parameterizations for the real and imaginary parts, for a total of 9 parameters, 3 for the real potential $V0$, R_R, a_R, 3 more to describe the imaginary volume potential W_V, R_V, a_V and the remaining 3 to describe the imaginary surface potential W_S, R_S, a_S. The potential used here is the latest iteration of the Avrigeanu Potential that has been in constant evolution since 2003 [24, 25, 26], and uses a large set of equations to calculate the necessary parameters. This potential has been derived from a series of experimental α-particle elastic scattering on $A \sim 100$.

TALYS [23] is a nuclear reaction software, that uses its own parameterization for the α–nucleus potential. This potential is based on the folding approach of Watanabe [27].

This analysis is necessary to test the theoretical predictions of the leading global α–nucleus potentials models. In the following sections, these models are applied to the two measured energies for the ^{64}Zn$(\alpha,\alpha)^{64}$Zn reaction by using the nuclear reactions program a0 [8] to calculate all the respective and necessary cross sections.

4.2.1 ^{64}Zn$(\alpha, \alpha)^{64}$Zn Global Potential at 12.075 MeV

Using the data resulting from the data analysis of the experimental results from the experiment performed at α-beam energy of 12.075 MeV in a ^{64}Zn target, and the aforementioned typical global α–nucleus potentials, such as McFadden [21], Avrigeanu [22] and TALYS [23], Fig. 4.1 was created, to visually depict the differences between the theoretical predictions and the experimental results.
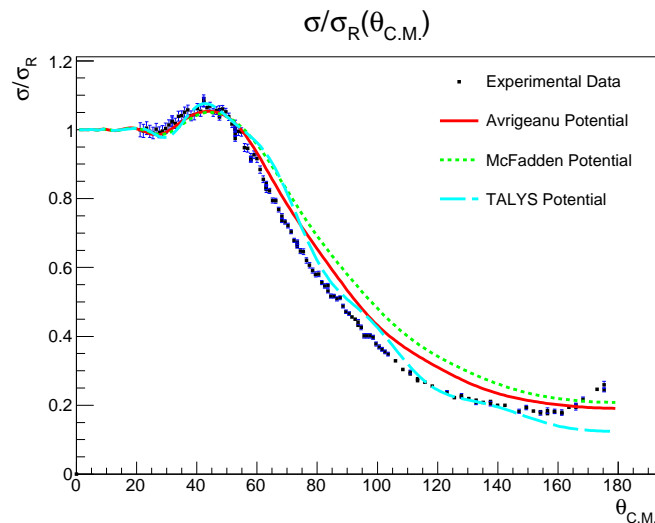
Figure 4.1: Global α nuclear potentials predictions for ^{64}Zn$(\alpha, \alpha)^{64}$Zn at 12.075 MeV. The most commonly used potentials are shown, i.e., McFadden, Avrigeanu and TALYS [21, 22, 23].

4.2.2 ^{64}Zn$(\alpha, \alpha)^{64}$Zn Global Potential at 16.137 MeV
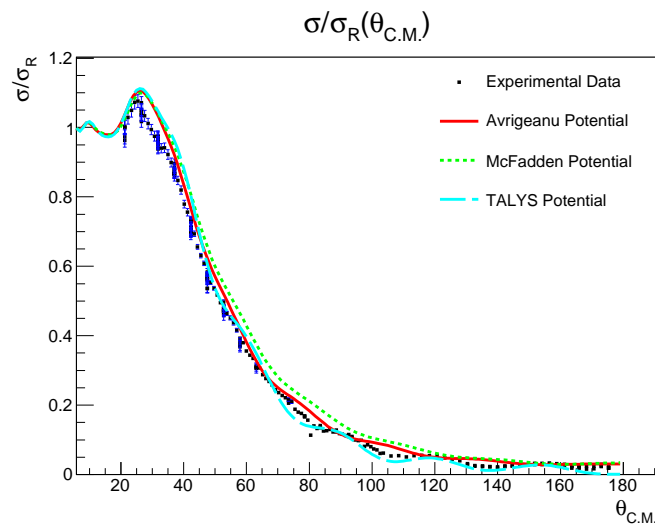
Figure 4.2: Global α nuclear potentials predictions for ^{64}Zn$(\alpha, \alpha)^{64}$Zn at 16.137 MeV. The most commonly used potentials are shown, i.e., McFadden, Avrigeanu and TALYS [21, 22, 23].

In order to get a clearer picture of the "goodness" of the description of the experimental data by the global α–nucleus potentials a χ^2_{red} test was performed for each global potential at the two measured energies. The results are shown in Table 4.1.

From the observation of the aforementioned Table 4.1 we can deduce that there isn't a overall best global α–nucleus potential for both measured energies, for the 12.075 MeV data the best is

^{64}Zn$(\alpha, \alpha)^{64}$Zn χ^2_{red} analysis		
Global Potential	12.075 MeV	16.137 MeV
Avrigeanu	71.7	313.3
McFadden	186.1	241.0
TALYS	56.1	386.8

Table 4.1: χ^2_{red} global α–nucleus potentials analysis for the ^{64}Zn.

the TALYS and for the 16.137 MeV is the McFadden global α–nucleus potential. However due to the high χ^2_{red} values obtained in this study, we cannot say that any of the considered global α–nucleus potential provides a sufficiently good description of the experimental data. As such a local α–nucleus potential analysis is necessary in order to find a α–nucleus potential that can better describe the experimental data.

4.3 ^{64}Zn$(\alpha, \alpha)^{64}$Zn Local α nuclear potential analysis

A local α–nucleus potential in contrast to the global α–nucleus potential only attempts to describe a single isotope, or a very limited mass region, at a given energy. It's parameters therefore only allow the estimation of the elastic α scattering cross section for a given isotope

The search for a local α–nucleus potential that describes the experimental scattering data with good accuracy, allowing for better predictions of the capture data is critical.

However due to the so called Family Problem, as seen in previous papers [28, 29], the search for a local α–nucleus potential can be quite challenging, due to the difficulties inherent in identifying the local α–nucleus potential that can describe the scattering data and the capture data of the nucleus in study.

The local α–nucleus potential analysis is the final step in the analysis of the data from the α scattering experiment. It allows the fitting of experimental data to a custom tailored optical potential, designed to provide the best possible description of the available experimental data. In this case, the available data is only for the α scattering data of the previously described experiment ^{64}Zn$(\alpha, \alpha)^{64}$Zn.

4.3.1 ^{64}Zn$(\alpha, \alpha)^{64}$Zn χ^2_{red} Analysis

The analysis was executed by program a0 [8], a tool developed to calculate and execute various analysis for elastic scattering reactions. However due to fitting and computational problems, it is not possible to fit all the parameters at the same time, therefore a sequence of fitting parameters and events is necessary.

The starting potential is a modified Avrigeanu *et al.* [22, 24, 25, 26], with the real part of the potential $V(r)$, $V0 = -169.5\ MeV$, $R_R = 1.27\ fm$, $a_R = 0.62\ fm$, and the imaginary potential $W(r)$ with volume parameters $W_V = -9.13\ MeV$, $R_V = 1.34\ fm$, $a_V = 0.50\ fm$, and surface parameters $W_S = -68.56\ MeV$, $R_S = 1.52\ fm$, $a_S = 0.43\ fm$.

In each iteration the depth of the real part of the potential $V0$ was progressively changed by parameter Fam, such that $V0 = -169.5 \times Fam$, with initial value of $Fam = 4$ (initial $V0 = 4 \times (-169.5)\ MeV$) and decreasing Fam in steps of 0.01, thus reducing $V0$ by steps of $1.695\ MeV$. Furthermore, 3 more steps were executed in each iteration, first the real radius R_R parameter was left free for the a0 program to fit, second the R_V was fitted together with R_R (departing from the value obtained in the previous step) and finally the last fit comprised R_R, R_V departing from the previous values obtained and releasing also W_V to perform a the fit.

Upon completing the analysis, the χ^2_{red} minima were selected, and the associated parameters are the families of α–nucleus potentials. The following Table 4.2 summarizes the obtained results.
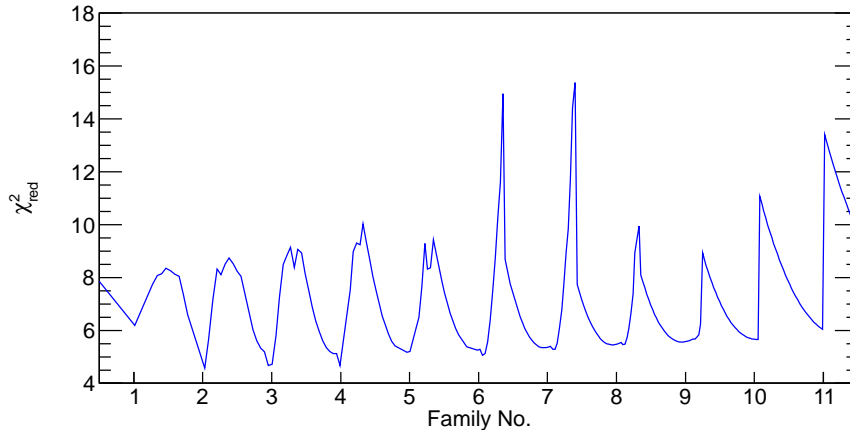
Figure 4.3: ^{64}Zn$(\alpha,\alpha)^{64}$Zn χ^2_{red} Analysis at 16.137 MeV using a strong WS surface potential.

Family No.	χ^2_{red}
1	6.2
2	4.6
3	4.7
4	4.7
5	5.2
6	5.1
7	5.3
8	5.4
9	5.6
10	5.7
11	6.0

Table 4.2: χ^2_{red} families extracted from Fig. 4.3

The results of Table 4.2, present a much better description of the experimental data, in comparison to the results obtained for the global α–nucleus potentials shown in Table 4.1.

4.3.2 ^{64}Zn$(\alpha,\alpha)^{64}$Zn Potential Families at 16.137 MeV

The χ^2_{red} analysis was performed with the experimental data at 16.137 MeV, therefore the obtained potential families are best fitted for this energy. The potential family with the best χ^2_{red} from Table 4.2 (family 2) is shown in Fig. 4.4. The other 10 potential families are not shown is this figure as they provide a very similar description of the experimental data.
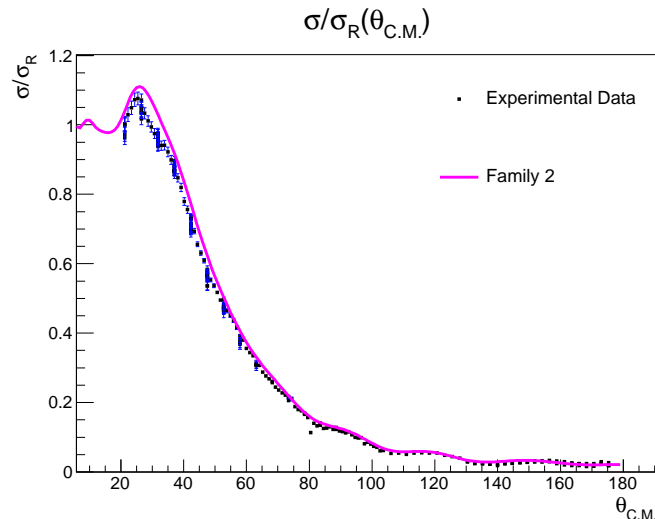
Figure 4.4: Local α nuclear potentials for ^{64}Zn$(\alpha,\alpha)^{64}$Zn at 16.137 MeV

The challenge now is to find a local α–nucleus potential that can describe the experimental data at 16 MeV and at 12 MeV. Therefore, applying the obtained families for the 16.137 MeV data to see if they can also describe the experimental data at 12.075 MeV, the result is in the following table:

Family No.	χ^2_{red}
1	118.9
2	118.8
3	125.1
4	123.7
5	127.3
6	125.9
7	126.7
8	129.7
9	130.3
10	129.7
11	140.4

Table 4.3: χ^2_{red} families extracted from Fig. 4.3 applied for the 12.075 MeV data.

The results shown in Table 4.3 indicate the families obtained from the 16.137 MeV fit do not describe very well the data at 12.075 MeV, however this new χ^2_{red} analysis shows that family 2 is again the best family of α–nucleus potential describing the experimental data. A plot of the α–nucleus potential family 2 is shown in Fig. 4.5.

The result shown in Fig. 4.5, highlights the problem indicated by the χ^2_{red} of Table 4.3. There is an overall underestimation of the experimental data, which may indicate the existence of an as yet unknown problem.

In order to clarify the situation, a χ^2_{red} was performed in order to search for local α–nucleus potentials among the 12.075MeV, the results can be seen in section 4.3.3.
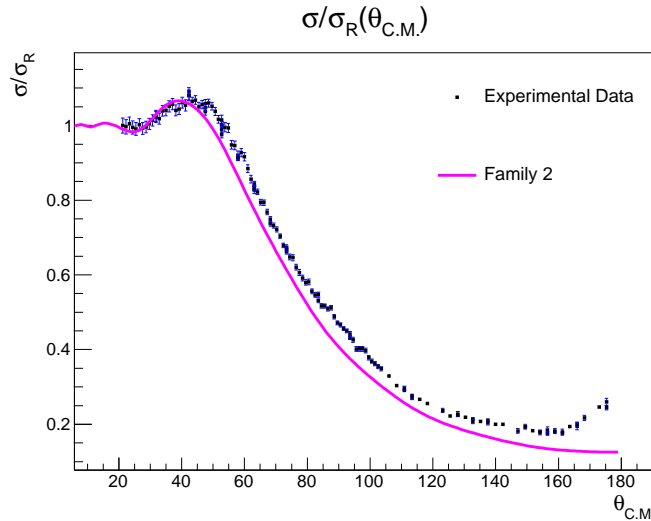
Figure 4.5: Local α nuclear potentials for ^{64}Zn$(\alpha, \alpha)^{64}$Zn at 12.075 MeV

4.3.3 ^{64}Zn$(\alpha, \alpha)^{64}$Zn Potential Families at 12.075 MeV

Due to the problems encountered by trying to fit the 12.075 MeV data with families obtained by a χ^2_{red} analysis on 16.137 MeV data, a new χ^2_{red} analysis, this time applied to 12.075 MeV data was executed. The starting family parameters are the same as for the 16.137 MeV data, described at the beginning of section 4.3.1. The results can be seen in Fig. 4.6.
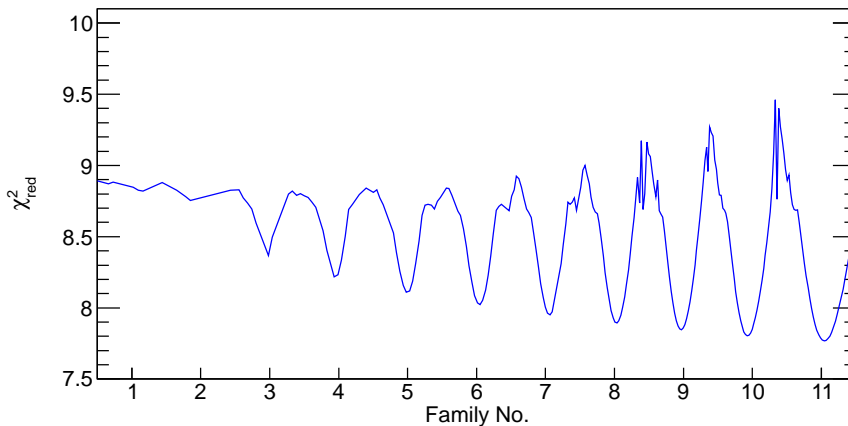
Figure 4.6: ^{64}Zn$(\alpha, \alpha)^{64}$Zn χ^2_{red} Analysis at 12.075 MeV using a strong WS surface potential.

The new χ^2_{red} analysis produced a new set of families. The results are shown in Table 4.4.

The results of Table 4.4, show a slightly worse description ($\chi^2_{red} \sim 8$) of the experimental data by the obtained minima from the χ^2_{red} analysis, comparing with the same approach done in the 16.137 MeV analysis ($\chi^2_{red} \sim 5$). Nevertheless a plot with the best family (family #11) arising from the χ^2_{red} analysis was built, and it's comparison with the experimental data at 12.075 MeV can be seen in Fig. 4.7.

The plot from Fig. 4.7 shows a reasonable description of the scattering data, as such, and applying the same reasoning from the previous section 4.3.2, the families obtained from this χ^2_{red} were used to fit the data at 16.137 MeV. The results are shown in Table 4.5.

Observing Table 4.5 we notice that the behaviour expressed in the previous section 4.3.2 repeats itself, and the families obtained by fitting the experimental data at 16.137 MeV don't reasonably describe the experimental data at 12.075 MeV, and vice-versa. However, for the

Family No.	χ^2_{red}
#1	8.4
#2	8.2
#3	8.1
#4	8.0
#5	8.0
#6	7.9
#7	8.7
#8	7.8
#9	7.8
#10	8.8
#11	7.8

Table 4.4: χ^2_{red} families extracted from Fig. 4.6
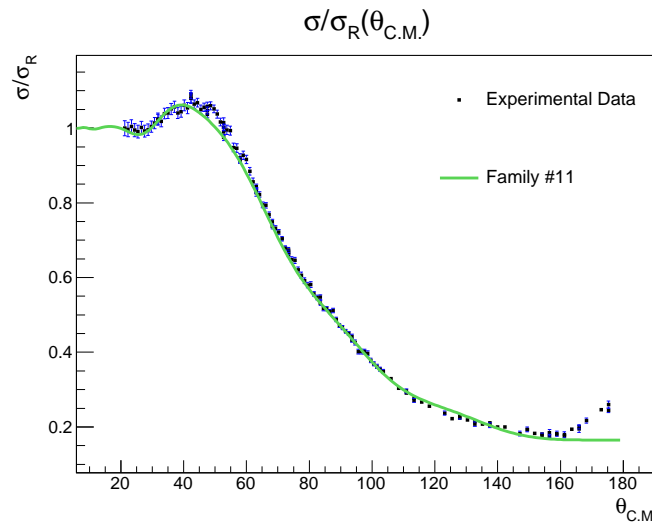
Figure 4.7: Local α nuclear potentials for ^{64}Zn$(\alpha, \alpha)^{64}$Zn at 12.075 MeV

Family No.	χ^2_{red}
#1	146.2
#2	146.2
#3	146.0
#4	145.7
#5	143.8
#6	142.0
#7	136.2
#8	140.3
#9	138.7
#10	132.7
#11	137.5

Table 4.5: χ^2_{red} families extracted from Fig. 4.6 applied for the 16.137 MeV data.

sake of consistency, the best family from this analysis was selected (family #10) and a plot was created to compare it to the experimental data at 16.137 MeV.

The plot in Fig. 4.8 shows an overestimation of the experimental data by family #10. The causes for this occurrence shall be discussed in the conclusions (Chapter 6), together with the
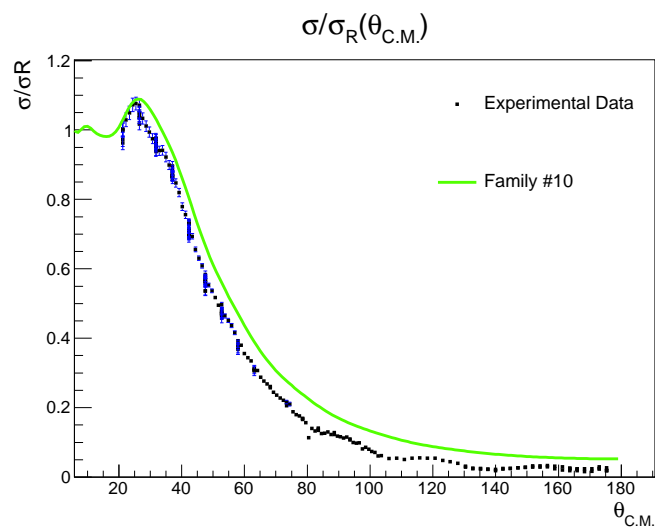
Figure 4.8: Local α nuclear potentials for ^{64}Zn$(\alpha, \alpha)^{64}$Zn at 16.137 MeV

underestimation of the data shown in Fig. 4.5.

Chapter 5

^{113}In and ^{115}In elastic α scattering experiment

There were 44 "Runs" performed , in a total of 11 hours of irradiation at 16,137 MeV for the ^{113}In. After that,the target was changed to ^{115}In, completing 43 "Runs", also for a total of 11 hours of irradiation.

After completing both irradiations at 16,137 MeV, the beam energy was changed to 19,49 MeV. We proceeded to irradiate the ^{113}In target at that beam energy, executing 47 "Runs", for a total of 19 hours and 30 minutes of target irradiation. To finalize the α particle scattering experiment, target was changed to the ^{115}In, completing 44 "Runs", for a total of 21 hours and 30 minutes of irradiation.

In total 284 "Runs" for 100 hours and 45 minutes of irradiation were necessary to complete the entire experiment (including the ^{64}Zn irradiation). The 284 "Runs" produced 2556 different spectra, as 9 detectors were used in each "Run".

5.1 ^{113}In$(\alpha, \alpha)^{113}$In Global potential analysis

The global α–nucleus potentials models considered for this analysis are the same as used for the ^{64}Zn$(\alpha, \alpha)^{64}$Zn experiment (L. McFadden and G. R. Satchler [21], M. Avrigeanu *et al.* [22] and TALYS [23]), with the necessary adjustments for the characteristics of the ^{113}In (M = 112.9041u and Z=49).

In accordance to the experiment we performed, 2 different energies where considered for the predictions of the global α–nucleus potentials. The predictions for α beam of energy of 16.137 MeV can be found in subsection 5.1.1 and for the 19.49 MeV α beam of energy in subsection 5.1.2.

5.1.1 $^{113}\text{In}(\alpha, \alpha)^{113}\text{In}$ Global Potential at 16.137 MeV

The results of the global α–nucleus potentials predictions for the α beam of energy 16.137 MeV can be observed in Fig. 5.1 superimposed with the experimental data for $^{113}\text{In}(\alpha, \alpha)^{113}\text{In}$ at that beam energy.

Figure 5.1: Global α nuclear potentials predictions for $^{113}\text{In}(\alpha, \alpha)^{113}\text{In}$ at 16.137 MeV. The most commonly used potentials are shown, i.e., McFadden, Avrigeanu and TALYS [21, 22, 23].

In Fig. 5.1 can observed the good agreement of the theoretical predictions of the considered global α–nucleus potentials for the experimental data taken at 16.137 MeV. A χ^2_{red} analysis was performed to test this assessment, and the results are shown in Table 5.1.

5.1.2 $^{113}\text{In}(\alpha, \alpha)^{113}\text{In}$ Global Potential at 19.49 MeV

The results of the global α–nucleus potentials predictions for the α beam of energy 19.49 MeV can be observed in Fig. 5.2 superimposed with the experimental data for ^{113}In at that beam energy.

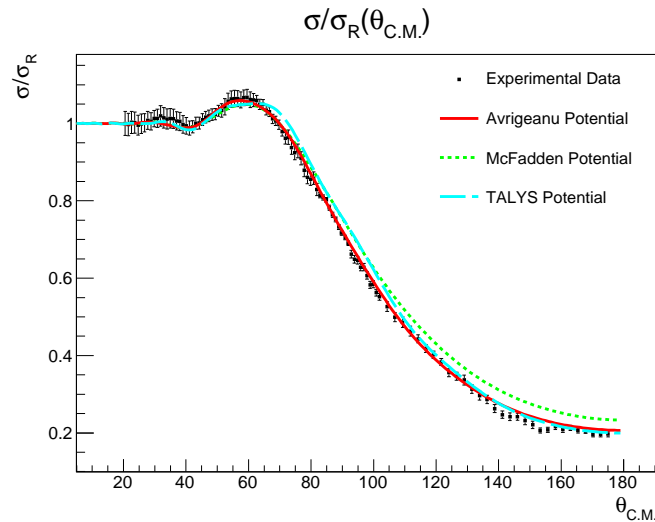Figure 5.2: Global α nuclear potentials predictions for $^{113}\text{In}(\alpha, \alpha)^{113}\text{In}$ at 19.49 MeV. The most commonly used potentials are shown, i.e., McFadden, Avrigeanu and TALYS [21, 22, 23].

In Fig. 5.2 the good agreement of the theoretical predictions of the global α–nucleus po-

tentials with the experimental data is evident, a χ^2_{red} analysis was also executed to confirm the goodness of the fit. The results of this analysis of the global α–nucleus potentials for the ^{113}In$(\alpha, \alpha)^{113}$In experimental data can be observed in Table 5.1.

^{113}In$(\alpha, \alpha)^{113}$In χ^2_{red} analysis		
Global Potential	16.137 MeV	19.49 MeV
Avrigeanu	1.478	1.277
McFadden	13.713	24.275
TALYS	7.814	9.850

Table 5.1: χ^2_{red} global α–nucleus potentials analysis for the ^{113}In$(\alpha, \alpha)^{113}$In.

The data shown by the χ^2_{red} analysis detailed in Table 5.1, clearly indicates that the best global α–nucleus potential for both measured energies is the Avrigeanu [22] potential. The TALYS potential provides a reasonable good description, while the McFadden potential provides the worst description of the experimental data.

5.2 ^{115}In$(\alpha, \alpha)^{115}$In Global potential analysis

The ^{115}In analysis, performed using the same global α–nucleus potentials as the previous analysis [21, 22, 23], modified to take into account the difference in mass (M = 114.9039u) of the ^{115}In isotope in relation to the ^{113}In isotope. The results can be seen in subsections 5.2.1 and 5.2.2.

5.2.1 ^{115}In$(\alpha, \alpha)^{115}$In Global Potential at 16.137 MeV

The results of the global α–nucleus potentials predictions for the α beam of energy 16.137 MeV can be observed in Fig. 5.3 superimposed with the experimental data for ^{115}In at that beam energy.
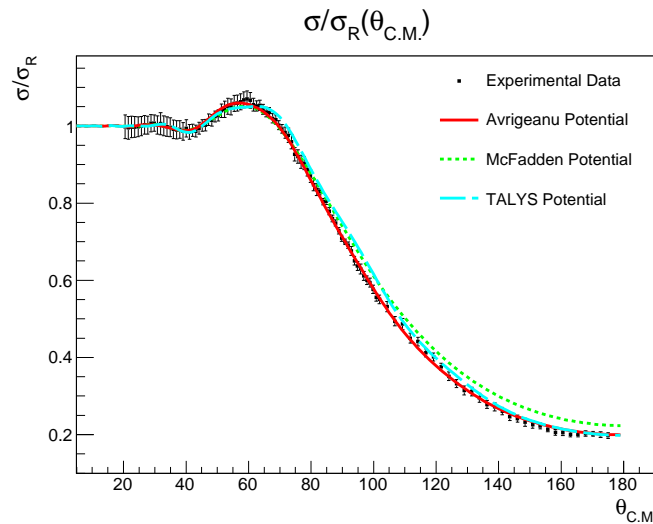
Figure 5.3: Global α nuclear potentials predictions for ^{115}In$(\alpha, \alpha)^{115}$In at 16.137 MeV. The most commonly used potentials are shown, i.e., McFadden, Avrigeanu and TALYS [21, 22, 23].

The considered global α–nucleus potentials provide a very good description of the experimental data, in order to discern the best global α–nucleus potential a χ^2_{red} was performed. The results of this χ^2_{red} analysis is shown in Table 5.2. The same approach was repeated for the 19.49 MeV experimental data, described in the following section.

5.2.2 ^{115}In$(\alpha,\alpha)^{115}$In Global Potential at 19.49 MeV

The results of the global α–nucleus potentials predictions for the α beam of energy 19.49 MeV can be observed in Fig. 5.4 superimposed with the experimental data for ^{115}In$(\alpha,\alpha)^{115}$In at that beam energy.
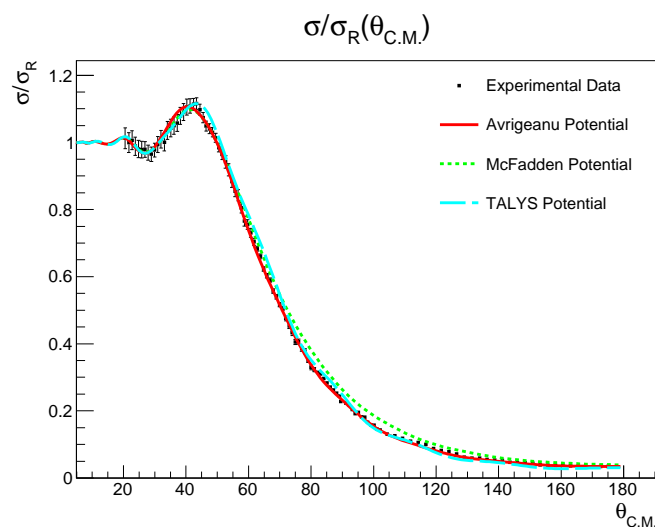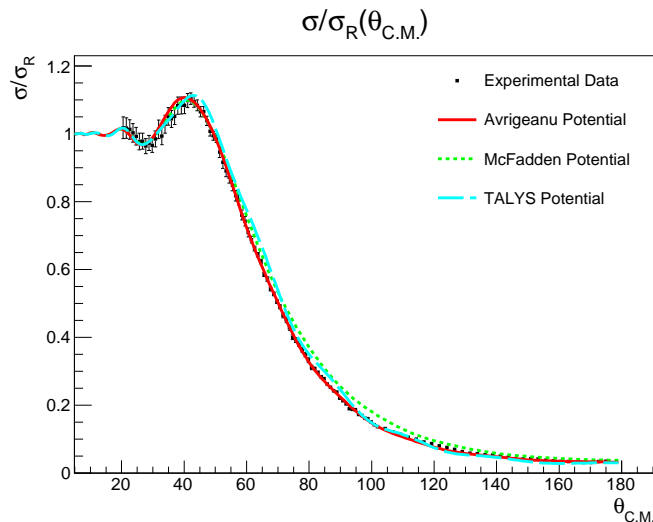

Figure 5.4: Global α nuclear potentials predictions for ^{115}In$(\alpha,\alpha)^{115}$In at 19.49 MeV. The most commonly used potentials are shown, i.e., McFadden, Avrigeanu and TALYS [21, 22, 23].

As was the case in the previous studies for ^{113}In and ^{115}In, the global α–nucleus potentials provide a good description of the experimental data, the χ^2_{red} analysis that shows this can be found in Table 5.2.

^{115}In$(\alpha,\alpha)^{115}$In χ^2_{red} analysis		
Global Potential	16.137 MeV	19.49 MeV
Avrigeanu	0.393	1.148
McFadden	6.109	26.684
TALYS	3.621	14.910

Table 5.2: χ^2_{red} global α–nucleus potentials analysis for the ^{115}In$(\alpha,\alpha)^{115}$In.

The previous analyses show a very good agreement of the global α–nucleus potentials to the experimental data, with special highlight to the results of the Avrigeanu [22] potential that consistently provide the best description for all cases. However a local α–nucleus potential search must be conducted in order to try to find families of potentials that can describe the experimental data with greater accuracy, or at least to find other possible parameterizations that can describe the experimental data for elastic scattering experiments and the experimental data for capture data experiments.

5.3 ^{113}In$(\alpha,\alpha)^{113}$In Local potential analysis

Following the same approach taken for the ^{64}Zn analysis, the search for a local α–nucleus potential was carried out for the ^{113}In experimental data.

5.3.1 ^{113}In$(\alpha,\alpha)^{113}$In χ^2_{red} Analysis

Departing from a slightly modified starting potential to take in account the different characteristics of the ^{113}In isotope, a χ^2_{red} analysis was undertaken to find the local α–nucleus potential families that best describe the experimental data. The results of this analysis can be seen in Fig. 5.5.
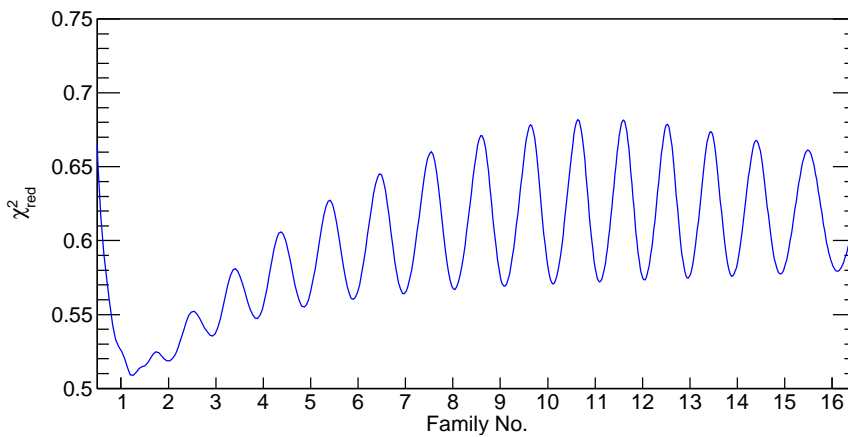
Figure 5.5: ^{113}In$(\alpha,\alpha)^{113}$In χ^2_{red} Analysis at 16.137 MeV using a strong WS surface potential.

From the analysis of Fig. 5.5, 16 different families of local α–nucleus potentials were found and their respective χ^2_{red} values can be observed in Table 5.3.

Family No.	χ^2_{red}
1	0.539
2	0.523
3	0.532
4	0.543
5	0.550
6	0.556
7	0.560
8	0.563
9	0.565
10	0.566
11	0.568
12	0.569
13	0.570
14	0.571
15	0.572
16	0.574

Table 5.3: χ^2_{red} families extracted from 5.5

From Table 5.3 it can be seen that in overall, all the families describe very well the experimental data, and it is very difficult to pinpoint the best possible family. In the next subsections

we can observe the description of the experimental data by a selected family, in this case family 3 was chosen.

5.3.2 ^{113}In$(\alpha, \alpha)^{113}$In Potential Families at 16.137 MeV

As stated previously, family 3 was chosen to be plotted alongside the experimental data. The differential cross section of the local α–nucleus potential described by family 3, was calculated by program a0 [8] (as all cross section in the previous sections), as described in section 1.1.5.
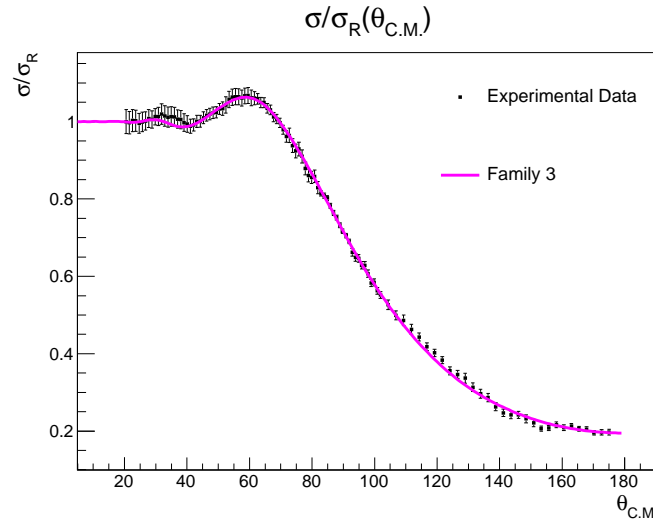
Figure 5.6: Local α nuclear potentials for ^{113}In$(\alpha, \alpha)^{113}$In at 16.137 MeV.

The excellent agreement between the experimental data and the calculated cross section from family 3 is evident. As such, it's necessary to test if this agreement applies itself to the other set of experimental data, the 19.49 MeV measurements.

5.3.3 ^{113}In$(\alpha, \alpha)^{113}$In Potential Families at 19.49 MeV

Applying the same local α–nucleus potential from the 16.137 MeV data, family 3 cross section was calculated for the 19.49 MeV data, and the results can be seen in Fig. 5.7.
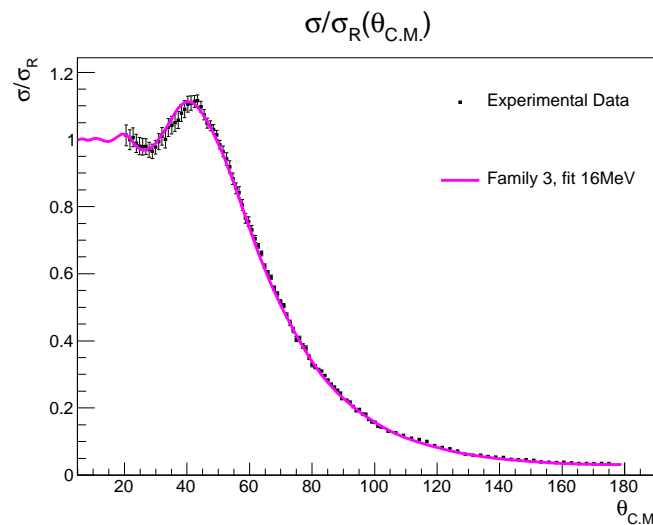
Figure 5.7: Local α nuclear potentials for ^{113}In$(\alpha, \alpha)^{113}$In at 19.49 MeV.

The excellent agreement between the experimental data and family 3, that was obtained from data at 16.137 MeV, proves that the search of local α–nucleus potentials that can describe the data at both energies is possible. To further solidify this point, a χ^2_{red} analysis of the families obtained at 16.137 MeV, applied to the data at 19.49 MeV, can be seen in Table 5.4.

Family No.	χ^2_{red}
1	3.232
2	2.102
3	1.760
4	1.849
5	2.038
6	2.215
7	2.362
8	2.465
9	2.512
10	2.497
11	2.489
12	2.423
13	2.367
14	2.316
15	2.269
16	2.220

Table 5.4: χ^2_{red} families extracted from 5.5, applied to the data at 19.49 MeV

The results from Table 5.4 show the excellent agreement of all the families of local α–nucleus potentials obtained at 16.137 MeV with the experimental data at 19.49 MeV. Also, when the analysis was repeated in reverse, i.e., a χ^2_{red} analysis, obtaining the corresponding local α–nucleus potentials at the 19.49 MeV, and then those families where applied to the data at 16.137 MeV, a very similar result was obtained, all the obtained families described very well the experimental data at both energies. This implies that without further information, for instance from capture data reaction, it is very difficult to the best family of α–nucleus potential. In this case, the safest conclusion we can make is that family 3 of local α–nucleus potentials is probably one of the best to describe the experimental data, however if we take a different starting potential and/or fitting process, it is not guaranteed that we can obtain the same family of local α–nucleus potentials.

5.4 ^{115}In$(\alpha,\alpha)^{115}$In Local potential analysis

The proceedings from ^{64}Zn and ^{113}In were repeated for this analysis.

5.4.1 ^{115}In$(\alpha,\alpha)^{115}$In χ^2_{red} Analysis

A χ^2_{red} analysis of local α–nucleus potentials was performed using program a0 [8] for the experimental data at 16.137 MeV. In Fig. 5.8 the results of that analysis can be seen.
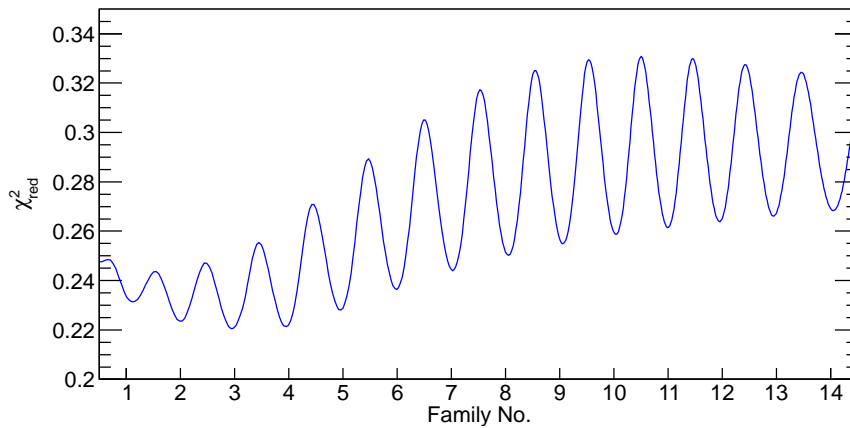
Figure 5.8: ^{115}In$(\alpha,\alpha)^{115}$In χ^2_{red} Analysis at 16.137 MeV using a strong WS surface potential.

From the minima of the χ^2_{red} analysis the parameters of the local α–nucleus potentials were extracted. The resulting families of α–nucleus potentials and their χ^2_{red} can be seen in Table 5.5

Family No.	χ^2_{red}
1#	0.230
2#	0.224
3#	0.223
4#	0.223
5#	0.227
6#	0.234
7#	0.242
8#	0.249
9#	0.254
10#	0.258
11#	0.262
12#	0.265
13#	0.268
14#	0.270

Table 5.5: χ^2_{red} families extracted from 5.8

In Table 5.5 we obtained the same behaviour as with the ^{113}In data at this energy, i.e., all the obtained local α–nucleus potentials families have very similar χ^2_{red}, making it difficult to conclude which family is the best to describe the experimental data.

5.4.2 ^{115}In Potential Families at 16.137 MeV

Taking into account the results from Table 5.5, family 3# was chosen, it's differential cross section was calculated using program a0, and the results where plotted alongside the experimen-

tal data at 16.137 MeV in Fig. 5.9.
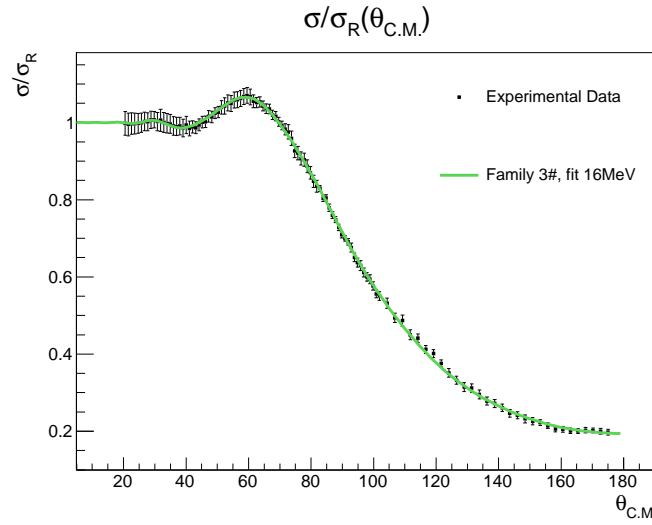
Figure 5.9: Local α nuclear potentials for ^{115}In$(\alpha, \alpha)^{115}$In at 16.137 MeV.

A very good agreement was again obtained between experimental data and the local α–nucleus potential , as such we repeat the procedure undertaken with ^{113}In, and use family 3# local α–nucleus potential in program a0, to calculate the differential cross section at 19.49 MeV.

5.4.3 ^{115}In$(\alpha, \alpha)^{115}$In Potential Families at 19.49 MeV

The result of the a0 calculation for family 3# at 19.49 MeV, can be seen in Fig. 5.10 plotted together with the experimental data at 19.49 MeV.
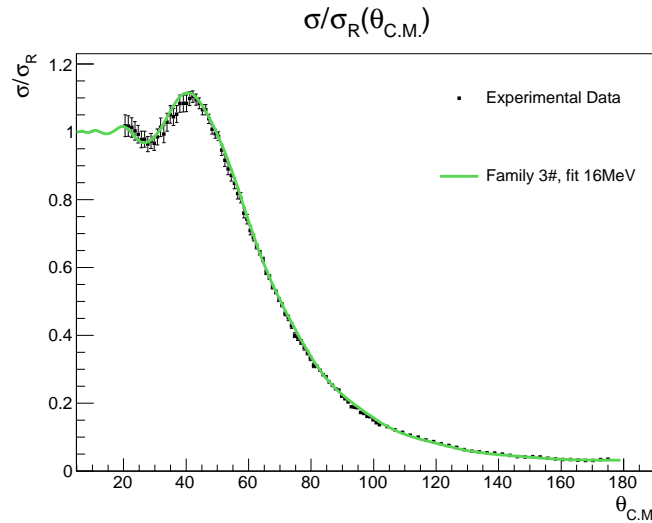
Figure 5.10: Local α nuclear potentials for ^{115}In$(\alpha, \alpha)^{115}$In at 19.49 MeV.

Once more, we can observe the excellent agreement between the experimental data and family 3#, obtained from data at 16.137 MeV. As with the case of ^{113}In we can not make a definite assessment of which family is the best without further data. However we found several local α–nucleus potentials families that can be used in further studies, should the necessary data be made available.

Chapter 6

Conclusions

In this work was presented the experimental details of α particles scattering in ^{64}Zn, ^{113}In and ^{115}In. The experimental setup and it's component were explained and described in detail. The experimental results were analysed and the extracted data was used to probe the validity of the global α–nucleus potentials and to perform a local α–nucleus potential search. The local α–nucleus potential probing was performed using the data obtained from the experimental data analysis, and the program used for the alpha-nuclear potential fitting was the a0 [8]. The resulting local α–nucleus potentials were then analysed, in order to solve the so-called "Family Problem".

The ^{64}Zn local α–nucleus potential search proved to be complicated, as the families obtained by fitting the 16.137 MeV data did not fit very well when applied to the 12.075 MeV data and vice-versa, however the families obtained at 16.771 MeV fitted the 12.075 MeV data slightly better than the other way around. The reasons for this slightly better description may rest with the fact that at 16.137 MeV, above the Coulomb barrier for the ^{64}Zn, the obtained potentials are more susceptible to variations of the parameters of the optical potential, and as such a minima found by a χ^2_{red} analysis is more robust than one found with the 12.075 MeV data. However, the reasons for these discrepancies between the fits can probably be attributed to a problem in my data analysis of the ^{64}Zn, there are some difficulties in the treatment of the experimental data which could not be totally corrected and have an influence in the outcome. Further study should be implemented in this matter, to try and solve the problems in the data analysis.

The χ^2_{red} analysis were executed with the scattering reaction experimental data, and the obtained families provide an overall good description of the experimental data, this it is not surprising, since the parameters were changed exactly to achieve this. However in this case it is not possible to find the correct potential family just by taking into account the scattering data. It is necessary to apply these potential families to alpha capture reactions and execute a χ^2_{red} analysis, this is beyond the scope of this Master Thesis, since the experimental data for the ^{64}Zn, ^{113}In and ^{115}In capture reactions ((α,γ), (α,n) and (α,p)) has only been recently published, and a comprehensive analysis was not carried out.

In conclusion, the reproduction of the data for the Indium isotopes is considerably better than for the ^{64}Zn case, however the global parameterizations considered in this work were developed for masses > 90, that and the factors previously mentioned are a big factor and thus it is perhaps not surprising that deviations from the data are more noticeable for the angular distribution of the reaction ^{64}Zn(α,α)^{64}Zn.

In a final note, it is possible to conclude, from the data here presented, that the experimental activity performed was successful, the obtained data has a very high quality, allowing for a very detailed analysis.

Acknowledgements

References

[1] W. Rapp, J. Görres, M. Wiescher, H. Schatz, and F. Käppeler, "Sensitivity of p-Process Nucleosynthesis to Nuclear Reaction Rates in a 25 M⊙ Supernova Model," *Astrophys. J.*, vol. 653, p. 474, 2006.

[2] E. M. Burbidge, G. R. Burbidge, W. A. Fowler, and F. Hoyle, "Synthesis of the elements in stars," *Rev. Mod. Phys.*, vol. 29, p. 547, Oct 1957.

[3] M. Arnould and S. Goriely, "The p-process of stellar nucleosynthesis: astrophysics and nuclear physics status," *Phys. Rep.*, vol. 384, p. 1, 2003.

[4] "http://www.nndc.bnl.gov/." National Nuclear Data Center.

[5] M. Rayet, M. Arnould, M. Hashimoto, N. Prantzos, and K. Nomoto, "The p-process in Type II supernovae," *Astronomy and Astrophysics*, vol. 298, p. 517, June 1995.

[6] T. Rauscher, "Branchings in the gamma process path revisited," *Phys. Rev. C*, vol. 73, no. 1, p. 015804, 2006.

[7] W. Hauser and H. Feshbach, "The inelastic scattering of neutrons," *Phys. Rev.*, vol. 87, pp. 366–373, Jul 1952.

[8] H. Abele and P. Mohr, "code a0₋, version 1.50," 2010. (unpublished).

[9] K. Krane, *Introductory Nuclear Physics*. John Wiley and Sons, 2 ed., 1988.

[10] "http://www.atomki.hu/atomki/accelerators/cyclotron/mgc20-en.html." Cyclotron MGC20-EN.

[11] G. G. Kiss, P. Mohr, Z. Fülöp, D. Galaviz, G. Gyürky, Z. Elekes, E. Somorjai, A. Kretschmer, K. Sonnabend, A. Zilges, and M. Avrigeanu, "High precision ^{89}Y$(\alpha,\alpha)^{89}$Y scattering at low energies," *Phys. Rev. C*, vol. 80, p. 045807, Oct 2009.

[12] G. G. Kiss, P. Mohr, Z. Fülöp, G. Gyürky, Z. Elekes, J. Farkas, E. Somorjai, C. Yalcin, D. Galaviz, R. T. Güray, N. Özkan, and J. Görres, "^{110,116}Cd$(\alpha, \alpha)^{110,116}$Cd elastic scattering and systematic investigation of elastic α scattering cross sections along the $Z = 48$ isotopic and $N = 62$ isotonic chains," *Phys. Rev. C*, vol. 83, p. 065807, 2011.

[13] "http://www.oerlikon.com/leyboldvacuum/univex/models₋350.html." Leybold UNIVEX 350 vacuum evaporator.

[14] J. F. Ziegler and J. P. Biersack, "http://www.srim.org/." SRIM - The Stopping and Range of Ions in Matter.

[15] "www.ortec-online.com/download/ultra.pdf." ORTEC ULTRA BU-013-050-500 Silicon Barrier Detectors.

[16] "http://www.caen.it/csite/caenprod.jsp?idmod=102&parent=12." CAEN N568B 16 Channel Programmable Spectroscopy Amplifier (Low Noise).

[17] "www.ortec-online.com/download/aspec-927.pdf." ORTEC ASPEC-927 Dual 16k Multi-channel Modules.

[18] O. Tarasov and D. Bazin, "LISE++: Radioactive beam production with in-flight separators," *Nuclear Instruments and Methods in Physics Research Section B: Beam Interactions with Materials and Atoms*, vol. 266, no. 19-20, pp. 4657 – 4664, 2008. Proceedings of the XVth International Conference on Electromagnetic Isotope Separators and Techniques Related to their Applications.

[19] R. Brun and F. Rademakers, "ROOT - An object oriented data analysis framework," *Nuclear Instruments and Methods in Physics Research Section A: Accelerators, Spectrometers, Detectors and Associated Equipment*, vol. 389, no. 1-2, pp. 81 – 86, 1997. New Computing Techniques in Physics Research V.

[20] G. Kiss, F. Zs., G. Gyürky, Z. Máté, E. Somorjai, D. Galaviz, A. Kretschmer, K. Sonnabend, and A. Zilges, "Study of the ^{106}Cd$(\alpha, \alpha)^{106}$Cd scattering at energies relevant to the p-process," *European Physics Journal*, vol. 27, p. 197, 2006.

[21] L. McFadden and G. R. Satchler, "Optical-model analysis of the scattering of 24.7 mev alpha particles," *Nucl. Phys.*, vol. 84, p. 177, 1966.

[22] M. Avrigeanu and V. Avrigeanu, "α-particle nuclear surface absorption below the coulomb barrier in heavy nuclei," *Phys. Rev. C*, vol. 82, p. 014606, Jul 2010.

[23] A. Koning, S. Hilaire, and M. Duijvestijn, "Talys-1.0," *Proceedings of the International Conference on Nuclear Data for Science and Technology*, 2008.

[24] M. Avrigeanu, W. von Oertzen, A. Plompen, and V. Avrigeanu, "Optical model potentials for α-particles scattering around the coulomb barrier on a$\sim$100 nuclei," *Nuclear Physics A*, vol. 723, no. 1-2, pp. 104 – 126, 2003.

[25] M. Avrigeanu, W. von Oertzen, and V. Avrigeanu, "On temperature dependence of the optical potential for alpha-particles at low energies," *Nucl. Phys.*, vol. A764, p. 246, 2006.

[26] M. Avrigeanu, A. Obreja, F. Roman, V. Avrigeanu, and W. von Oertzen, "Complementary optical-potential analysis of α-particle elastic scattering and induced reactions at low energies," *Atomic Data and Nuclear Data Tables*, vol. 95, no. 4, pp. 501 – 532, 2009.

[27] S. Watanabe, "High energy scattering of deuterons by complex nuclei," *Nuclear Physics*, vol. 8, no. 0, pp. 484 – 492, 1958.

[28] P. Mohr, T. Rauscher, H. Oberhummer, Z. Máté, Z. Fülöp, E. Somorjai, M. Jaeger, and G. Staudt, "^{144}Sm–α optical potential at astrophysically relevant energies derived from ^{144}Sm$(\alpha,\alpha)^{144}$Sm elastic scattering," *Phys. Rev. C*, vol. 55, p. 1523, 1997.

[29] Z. Fülöp, G. Gyürky, Z. Máté, E. Somorjai, L. Zolnai, D. Galaviz, M. Babilon, P. Mohr, A. Zilges, T. Rauscher, H. Oberhummer, and G. Staudt, "^{92}Mo$(\alpha, \alpha)^{92}Mo$ scattering, the $^{92}Mo-\alpha$ optical potential, and the $^{96}Ru(\gamma, \alpha)^{92}Mo$ reaction rate at astrophysically relevant energies," *Phys. Rev. C*, vol. 64, p. 065805, Nov 2001.

Annex A

Energy Calibration

In the following Table A.1, Max Chan contains the channel number of the elastic (ineslastic) peak of ^{64}Zn, ^{64}Zn(0.9916), ^{16}O, ^{12}C, ^{12}C(4.4389) and ^{16}O(6.0494) in that order. All energies are in MeV and were calculated with Eq. 2.3.

D1		D2		D3	
Max Chn	Max E.	Max Chn	Max E.	Max Chn	Max E.
1030	16.03	898	15.96	977	15.88
985	15.04	834	14.97	911	14.90
1019	15.67	865	15.41	926	15.10
1005	15.51	851	15.16	906	14.76
699	11.01	594	10.70	627	10.34
594	9.51		9.29	547	9.03
D4		D5		D6	
Max Chn	Max E.	Max Chn	Max E.	Max Chn	Max E.
970	15.79	972	15.68	1022	16.03
904	14.81		14.70	957	15.04
903	14.74	887	14.35	998	15.67
876	14.29	852	13.78	989	15.51
601	9.93	578	9.48	695	11.01
485	8.74	505	8.42	591	9.51
D7		M1		M2	
Max Chn	Max E.	Max Chn	Max E.	Max Chn	Max E.
967	15.88	1263	16.08	1117	16.08
905	14.90		15.09		15.09
918	15.10	1244	15.88	1096	15.88
898	14.76	1219	15.79		15.79
622	10.34	880	11.26	775	11.26
548	9.03		9.68		9.68

Table A.1: Energy Calibration

Angular Calibration
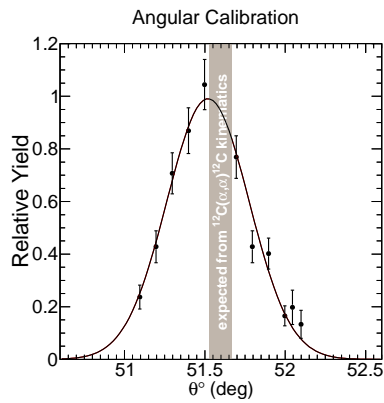
(a) Angular Calibration for detector pair D1-D6.
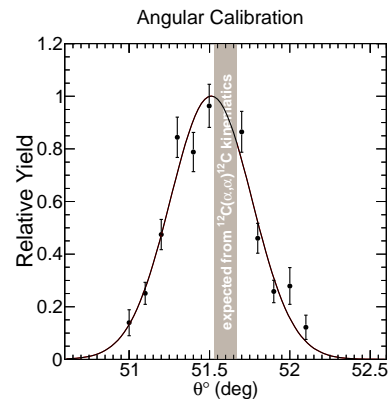
(b) Angular Calibration for detector pair D1-D7.
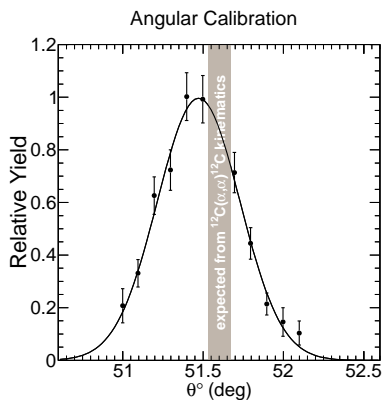
(c) Angular Calibration for detector pair D2-D6.
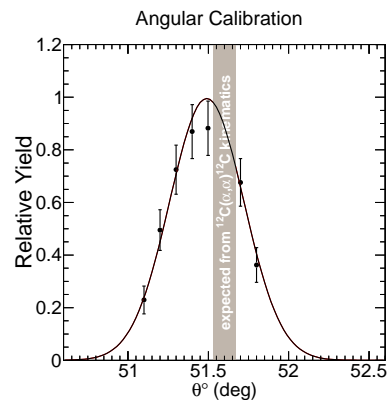
(d) Angular Calibration for detector pair D3-D6.

Figure A.1: Angular Calibrations of the different detector pairs.
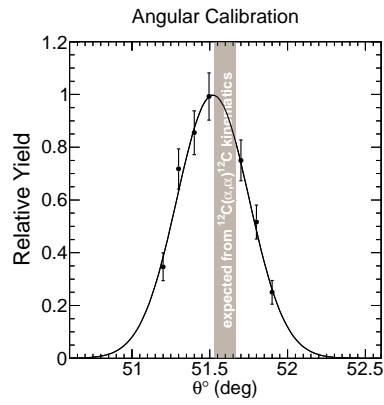
(a) Angular Calibration for detector pair D3-D7.
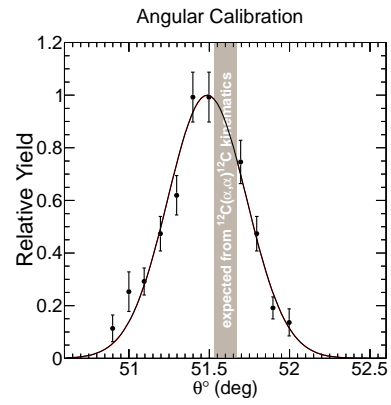
(b) Angular Calibration for detector pair D4-D6.
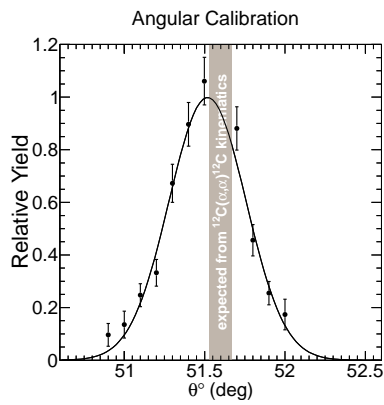
(c) Angular Calibration for detector pair D5-D6.
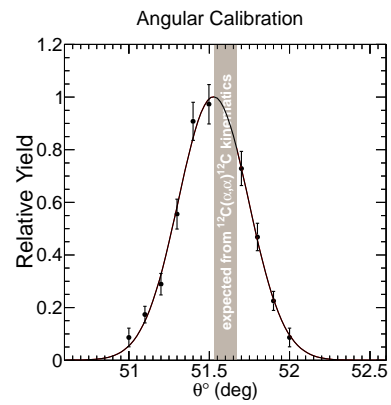
(d) Angular Calibration for detector pair D5-D7.

Figure A.2: Angular Calibrations of the different detector pairs.

Annex B

^{64}Zn Experimental Data at 16.137 MeV

$\theta_{C.M.}(°)$	$\left(\frac{d\sigma}{d\Omega}\right)(\vartheta)$	$\left(\frac{d\sigma}{d\Omega}\right)(\vartheta)$ error
21,227	0,963	1,951E-02
21,227	0,973	1,985E-02
21,227	1,004	2,047E-02
21,227	1,001	2,024E-02
21,227	0,999	2,032E-02
22,285	1,029	1,990E-02
23,344	1,049	1,946E-02
24,401	1,072	1,913E-02
25,459	1,076	1,836E-02
26,516	1,037	1,703E-02
26,516	1,017	1,711E-02
26,516	1,042	1,710E-02
26,516	1,035	1,736E-02
26,516	1,071	1,765E-02
26,516	1,051	1,716E-02
26,516	1,048	1,740E-02
27,572	1,033	1,638E-02
28,628	1,011	1,555E-02
29,684	0,994	1,480E-02
30,739	0,975	1,404E-02
31,793	0,938	1,347E-02
31,793	0,941	1,440E-02
31,793	0,972	1,390E-02
31,793	0,960	1,459E-02
31,793	0,967	1,395E-02
31,793	0,951	1,467E-02
31,793	0,960	1,339E-02
31,793	0,953	1,343E-02
31,793	0,960	1,422E-02
31,793	0,972	1,522E-02
31,793	0,957	1,365E-02
31,793	0,975	1,470E-02

Table B.1: ^{64}Zn Experimental data at 16.137 MeV

$\theta_{C.M.}(°)$	$\left(\frac{d\sigma}{d\Omega}\right)(\vartheta)$	$\left(\frac{d\sigma}{d\Omega}\right)(\vartheta)$ error
32,847	0,940	1,354E-02
33,901	0,941	1,387E-02
34,954	0,922	1,386E-02
36,006	0,899	1,292E-02
37,057	0,866	1,187E-02
37,057	0,867	1,349E-02
37,057	0,857	1,170E-02
37,057	0,867	1,340E-02
37,057	0,880	1,218E-02
37,057	0,869	1,379E-02
37,057	0,885	1,207E-02
37,057	0,867	1,345E-02
37,057	0,867	1,141E-02
37,057	0,865	1,269E-02
37,057	0,896	1,295E-02
37,057	0,872	1,178E-02
37,057	0,875	1,335E-02
38,108	0,848	1,196E-02
39,159	0,820	1,171E-02
40,208	0,779	1,109E-02
41,258	0,756	1,055E-02
42,306	0,702	1,043E-02
42,306	0,729	1,321E-02
42,306	0,714	1,046E-02
42,306	0,705	1,270E-02
42,306	0,701	1,064E-02
42,306	0,690	1,305E-02
42,306	0,729	1,068E-02
42,306	0,697	1,273E-02
42,306	0,714	1,038E-02
42,306	0,698	1,246E-02
42,306	0,736	8,217E-03
42,306	0,713	9,816E-03
42,306	0,695	1,166E-02
42,306	0,728	9,989E-03
42,306	0,713	1,030E-02
42,306	0,705	1,250E-02
43,353	0,694	7,611E-03
44,400	0,656	7,098E-03
45,447	0,631	6,723E-03
46,492	0,608	6,371E-03
47,537	0,562	9,903E-03
47,537	0,565	1,297E-02
47,537	0,574	1,047E-02
47,537	0,568	1,355E-02
47,537	0,584	1,021E-02
47,537	0,536	1,264E-02
47,537	0,568	9,842E-03
47,537	0,560	1,266E-02
47,537	0,577	5,953E-03
$\theta_{C.M.}(°)$	$\left(\frac{d\sigma}{d\Omega}\right)(\vartheta)$	$\left(\frac{d\sigma}{d\Omega}\right)(\vartheta)$ error

Table B.2: ^{64}Zn Experimental data at 16.137 MeV

$\theta_{C.M.}(^\circ)$	$\left(\frac{d\sigma}{d\Omega}\right)(\vartheta)$	$\left(\frac{d\sigma}{d\Omega}\right)(\vartheta)$ error
47,537	0,564	9,742E-03
47,537	0,537	1,224E-02
48,581	0,553	5,630E-03
49,624	0,536	5,368E-03
50,666	0,517	5,085E-03
51,708	0,495	4,843E-03
52,748	0,470	1,078E-02
52,748	0,469	1,454E-02
52,748	0,478	1,046E-02
52,748	0,458	1,367E-02
52,748	0,466	1,006E-02
52,748	0,471	1,355E-02
52,748	0,486	4,652E-03
52,748	0,497	6,661E-03
52,748	0,477	1,013E-02
52,748	0,474	1,356E-02
53,788	0,464	6,209E-03
54,827	0,451	5,988E-03
55,865	0,437	5,757E-03
56,903	0,416	5,439E-03
57,939	0,384	1,079E-02
57,939	0,368	1,443E-02
57,939	0,377	1,041E-02
57,939	0,372	1,401E-02
57,939	0,393	5,114E-03
58,975	0,380	4,910E-03
60,009	0,355	4,588E-03
61,043	0,344	4,360E-03
62,076	0,334	4,264E-03
63,107	0,306	3,466E-03
63,107	0,309	1,083E-02
63,107	0,307	1,488E-02
63,107	0,313	4,795E-03
63,107	0,312	3,950E-03
64,138	0,307	4,798E-03
65,168	0,288	4,415E-03
66,197	0,277	4,240E-03
67,225	0,268	4,122E-03
68,252	0,261	3,375E-03
68,252	0,258	3,999E-03
69,278	0,244	3,756E-03
70,303	0,236	3,232E-03
71,327	0,228	2,804E-03
72,350	0,222	2,720E-03
73,372	0,213	3,269E-03
73,372	0,215	3,493E-03
73,372	0,206	2,451E-03
73,372	0,216	5,352E-03
74,393	0,210	5,328E-03
75,413	0,188	4,770E-03

Table B.3: ^{64}Zn Experimental data at 16.137 MeV

$\theta_{C.M.}(^\circ)$	$\left(\frac{d\sigma}{d\Omega}\right)(\vartheta)$	$\left(\frac{d\sigma}{d\Omega}\right)(\vartheta)$ error
76,432	0,180	4,550E-03
77,449	0,176	4,442E-03
78,466	0,169	3,129E-03
78,466	0,166	3,224E-03
78,466	0,169	4,297E-03
79,482	0,156	3,971E-03
80,497	0,114	2,902E-03
81,510	0,140	2,810E-03
82,523	0,133	2,688E-03
83,534	0,138	3,262E-03
83,534	0,141	3,173E-03
83,534	0,135	2,521E-03
84,544	0,125	2,744E-03
85,554	0,126	2,727E-03
86,562	0,130	2,796E-03
87,569	0,123	2,477E-03
88,575	0,129	3,302E-03
88,575	0,123	2,819E-03
89,580	0,118	2,413E-03
90,584	0,116	2,909E-03
91,586	0,113	2,239E-03
92,588	0,116	3,063E-03
93,589	0,110	3,226E-03
93,589	0,107	1,995E-03
94,588	0,100	3,172E-03
95,586	0,097	3,101E-03
96,584	0,099	3,148E-03
97,580	0,081	2,590E-03
98,575	0,085	3,015E-03
99,569	0,080	2,538E-03
100,562	0,074	2,968E-03
101,554	0,071	2,250E-03
102,544	0,061	2,835E-03
103,534	0,061	1,910E-03
106,003	0,054	1,291E-03
108,466	0,054	1,218E-03
110,922	0,050	1,306E-03
113,372	0,055	1,279E-03
115,815	0,056	1,532E-03
118,252	0,054	1,413E-03
120,683	0,054	1,525E-03
123,107	0,048	1,334E-03
125,526	0,045	1,406E-03
127,939	0,039	1,231E-03
130,346	0,029	2,158E-03
130,346	0,031	1,148E-03
132,748	0,026	1,668E-03
132,748	0,024	1,010E-03

Table B.4: ^{64}Zn Experimental data at 16.137 MeV

$\theta_{C.M.}(^\circ)$	$\left(\frac{d\sigma}{d\Omega}\right)(\vartheta)$	$\left(\frac{d\sigma}{d\Omega}\right)(\vartheta)$ error
135,145	0,023	1,981E-03
135,145	0,025	1,043E-03
137,537	0,023	1,607E-03
137,537	0,022	9,835E-04
139,924	0,019	1,935E-03
139,924	0,022	1,078E-03
142,306	0,025	1,816E-03
142,306	0,023	1,104E-03
144,684	0,025	2,199E-03
144,684	0,025	1,122E-03
147,057	0,026	1,842E-03
147,057	0,027	1,169E-03
149,427	0,027	2,309E-03
149,427	0,028	1,200E-03
151,793	0,029	1,911E-03
151,793	0,032	1,264E-03
154,156	0,029	1,431E-03
154,156	0,032	1,324E-03
156,516	0,030	1,530E-03
156,516	0,033	1,527E-03
158,873	0,024	1,314E-03
158,873	0,032	1,318E-03
161,227	0,021	1,269E-03
161,227	0,029	1,438E-03
163,578	0,018	1,222E-03
163,578	0,026	1,277E-03
163,578	0,025	1,054E-03
163,578	0,023	1,021E-03
165,928	0,018	1,288E-03
165,928	0,023	1,366E-03
165,928	0,022	1,132E-03
165,928	0,024	1,030E-03
168,276	0,016	1,118E-03
168,276	0,024	1,196E-03
170,623	0,017	1,194E-03
170,623	0,024	1,342E-03
172,968	0,023	1,303E-03
172,968	0,029	1,290E-03
172,968	0,025	1,174E-03
172,968	0,024	1,163E-03
175,313	0,027	1,477E-03
175,313	0,018	1,145E-03
175,313	0,019	1,159E-03
175,313	0,020	1,050E-03

Table B.5: ^{64}Zn Experimental data at 16.137 MeV

^{64}Zn Experimental Data at 12.075 MeV

$\theta_{C.M.}(°)$	$\left(\frac{d\sigma}{d\Omega}\right)(\vartheta)$	$\left(\frac{d\sigma}{d\Omega}\right)(\vartheta)$ error
21,227	1,000	2,029E-02
22,285	0,997	1,927E-02
23,344	1,004	1,853E-02
24,401	0,995	1,762E-02
25,459	0,991	1,696E-02
26,516	1,002	1,653E-02
27,572	0,992	1,581E-02
28,628	0,996	1,548E-02
29,684	1,004	1,509E-02
30,739	1,014	1,482E-02
31,793	1,023	1,449E-02
31,793	1,025	1,504E-02
32,847	1,018	1,456E-02
33,901	1,039	1,431E-02
34,954	1,040	1,431E-02
36,006	1,051	1,482E-02
37,057	1,057	1,472E-02
38,108	1,041	1,439E-02
39,159	1,044	1,485E-02
40,208	1,061	1,472E-02
41,258	1,054	1,463E-02
42,306	1,090	1,098E-02
42,306	1,080	1,213E-02
42,306	1,080	1,457E-02
43,353	1,064	1,183E-02
44,400	1,068	1,166E-02
45,447	1,050	1,129E-02
46,492	1,056	1,115E-02
47,537	1,048	9,540E-03
47,537	1,037	9,459E-03
47,537	1,058	1,099E-02
48,581	1,060	1,081E-02
49,624	1,052	1,063E-02
50,666	1,038	1,040E-02
51,708	1,016	9,932E-03
52,748	1,002	8,415E-03
52,748	0,975	8,277E-03
52,748	1,002	8,658E-03
52,748	0,990	9,567E-03
52,748	1,015	1,239E-02
53,788	0,995	1,228E-02
54,827	0,993	1,212E-02
55,865	0,948	1,161E-02
56,903	0,946	1,146E-02
57,939	0,914	7,356E-03
57,939	0,914	7,668E-03

Table B.6: ^{64}Zn Experimental data at 12.075 MeV

$\theta_{C.M.}(^{\circ})$	$\left(\frac{d\sigma}{d\Omega}\right)(\vartheta)$	$\left(\frac{d\sigma}{d\Omega}\right)(\vartheta)$ error
57,939	0,920	1,111E-02
58,975	0,927	1,099E-02
60,009	0,916	1,091E-02
61,043	0,885	1,061E-02
62,076	0,856	1,000E-02
63,107	0,833	6,898E-03
63,107	0,833	7,067E-03
63,107	0,844	6,925E-03
63,107	0,827	9,649E-03
64,138	0,822	7,256E-03
65,168	0,795	7,565E-03
66,197	0,793	7,446E-03
67,225	0,768	7,274E-03
68,252	0,737	6,501E-03
68,252	0,749	7,121E-03
69,278	0,732	6,814E-03
70,303	0,722	6,994E-03
71,327	0,704	6,012E-03
72,350	0,679	5,953E-03
73,372	0,662	6,038E-03
73,372	0,668	5,868E-03
73,372	0,674	6,779E-03
74,393	0,648	7,421E-03
75,413	0,646	8,188E-03
76,432	0,621	7,867E-03
77,449	0,606	7,776E-03
78,466	0,591	7,641E-03
79,482	0,580	7,289E-03
80,497	0,581	7,660E-03
81,510	0,556	6,272E-03
82,523	0,546	6,353E-03
83,534	0,547	6,384E-03
83,534	0,532	6,241E-03
84,544	0,517	6,049E-03
85,554	0,517	5,741E-03
86,562	0,509	5,870E-03
87,569	0,512	5,889E-03
88,575	0,488	5,713E-03
89,580	0,472	5,352E-03
90,584	0,466	5,386E-03
91,586	0,456	5,117E-03
92,588	0,450	5,195E-03
93,589	0,432	4,996E-03
93,589	0,441	7,173E-03
94,588	0,426	6,872E-03
95,586	0,402	6,281E-03
96,584	0,402	6,489E-03
97,580	0,402	6,480E-03

Table B.7: ^{64}Zn Experimental data at 12.075 MeV

$\theta_{C.M.}(^\circ)$	$\left(\frac{d\sigma}{d\Omega}\right)(\vartheta)$	$\left(\frac{d\sigma}{d\Omega}\right)(\vartheta)$ error
98,575	0,397	6,407E-03
99,569	0,378	5,929E-03
100,562	0,369	5,929E-03
101,554	0,362	5,618E-03
102,544	0,355	5,686E-03
103,534	0,349	5,526E-03
106,003	0,329	3,376E-03
108,466	0,304	2,992E-03
110,922	0,291	3,221E-03
110,922	0,297	5,403E-03
113,372	0,277	2,896E-03
113,372	0,271	5,105E-03
115,815	0,267	3,417E-03
118,252	0,255	3,066E-03
120,683	0,243	5,918E-03
123,107	0,237	5,750E-03
125,526	0,222	3,184E-03
127,939	0,228	6,289E-03
127,939	0,224	2,917E-03
130,346	0,219	4,533E-03
132,748	0,215	4,580E-03
132,748	0,207	6,020E-03
135,145	0,208	4,418E-03
137,537	0,211	4,537E-03
137,537	0,205	6,543E-03
139,924	0,200	4,726E-03
142,306	0,200	4,802E-03
147,057	0,182	6,108E-03
149,427	0,193	6,404E-03
149,427	0,193	4,574E-03
151,793	0,183	4,512E-03
154,156	0,181	4,002E-03
154,156	0,177	6,047E-03
156,516	0,184	8,257E-03
156,516	0,175	4,946E-03
158,873	0,180	3,916E-03
158,873	0,182	6,587E-03
161,227	0,179	7,975E-03
161,227	0,176	4,852E-03
163,578	0,194	4,354E-03
165,928	0,194	8,894E-03
165,928	0,200	5,545E-03
168,276	0,217	6,889E-03
172,968	0,246	4,640E-03
175,313	0,260	9,657E-03
175,313	0,244	5,679E-03

Table B.8: ^{64}Zn Experimental data at 12.075 MeV